

1   **A fluorescent sensor for spatiotemporally resolved endocannabinoid dynamics *in*  
2   *vitro* and *in vivo***

3  
4   Ao Dong<sup>1,2,3</sup>, Kaikai He<sup>1,2</sup>, Barna Dudok<sup>4</sup>, Jordan S Farrell<sup>4</sup>, Wuqiang Guan<sup>5</sup>, Daniel J  
5   Liput<sup>6,7</sup>, Henry L Puhl<sup>7</sup>, Ruyi Cai<sup>1,2</sup>, Jiali Duan<sup>1,2</sup>, Eddy Albaran<sup>8</sup>, Jun Ding<sup>9</sup>, David M  
6   Lovinger<sup>6</sup>, Bo Li<sup>5</sup>, Ivan Soltesz<sup>4</sup>, & Yulong Li<sup>1,2,3,10,\*</sup>

7

8   <sup>1</sup>State Key Laboratory of Membrane Biology, Peking University School of Life Sciences,  
9   Beijing, China;

10   <sup>2</sup>PKU-IDG/McGovern Institute for Brain Research, Beijing, China;

11   <sup>3</sup>Peking-Tsinghua Center for Life Sciences, Academy for Advanced Interdisciplinary  
12   Studies, Peking University, Beijing, China;

13   <sup>4</sup>Department of Neurosurgery, Stanford University, Palo Alto, CA, USA;

14   <sup>5</sup>Cold Spring Harbor Laboratory, Cold Spring Harbor, NY, USA;

15   <sup>6</sup>Laboratory for Integrative Neuroscience, National Institute on Alcohol Abuse and  
16   Alcoholism, Bethesda, MD, USA;

17   <sup>7</sup>Laboratory of Molecular Physiology, National Institute on Alcohol Abuse and Alcoholism,  
18   Bethesda, MD, USA;

19   <sup>8</sup>Neuroscience PhD Program, Stanford University, Palo Alto, CA, USA;

20   <sup>9</sup>Department of Neurosurgery, Department of Neurology, Stanford University School of  
21   Medicine, Palo Alto, CA, USA;

22   <sup>10</sup>Chinese Institute for Brain Research, Beijing, China.

23

24   \*Correspondence should be addressed to Y.L. (yulongli@pku.edu.cn).

25

26   **Endocannabinoids (eCBs) are retrograde neuromodulators that play an important  
27   role in a wide range of physiological processes; however, the release and *in vivo*  
28   dynamics of eCBs remain largely unknown, due in part to a lack of suitable probes  
29   capable of detecting eCBs with sufficient spatiotemporal resolution. Here, we  
30   developed a new eCB sensor called GRAB<sub>eCB2.0</sub>. This genetically encoded sensor  
31   consists of the human CB1 cannabinoid receptor fused to circular-permuted EGFP,  
32   providing cell membrane trafficking, second-resolution kinetics, high specificity for  
33   eCBs, and a robust fluorescence response at physiological eCB concentrations.  
34   Using the GRAB<sub>eCB2.0</sub> sensor, we monitored evoked changes in eCB dynamics in  
35   both cultured neurons and acute brain slices. Interestingly, in cultured neurons we  
36   also observed spontaneous compartmental eCB transients that spanned a distance  
37   of approximately 11 μm, suggesting constrained, localized eCB signaling. Moreover,  
38   by expressing GRAB<sub>eCB2.0</sub> in the mouse brain, we readily observed foot shock-  
39   elicited and running-triggered eCB transients in the basolateral amygdala and  
40   hippocampus, respectively. Lastly, we used GRAB<sub>eCB2.0</sub> in a mouse seizure model  
41   and observed a spreading wave of eCB release that followed a Ca<sup>2+</sup> wave through  
42   the hippocampus. Thus, GRAB<sub>eCB2.0</sub> is a robust new probe for measuring the  
43   dynamics of eCB release under both physiological and pathological conditions.**

44

45 Cannabis derivatives have long been used for medicinal and recreational purposes across  
46 many cultures in formulations such as marijuana and hashish<sup>1</sup>. Bioactive compounds in  
47 cannabis, phytocannabinoids, exert their function by “hijacking” the body’s endogenous  
48 cannabinoid (endocannabinoid, or eCB) system. The biological function of eCBs—majorly  
49 two lipid metabolites 2-arachidonoylglycerol (2-AG) and anandamide (AEA)—is primarily  
50 mediated by the activation of type 1 and type 2 cannabinoid receptors (CB1R and CB2R)<sup>2</sup>.  
51 eCBs are widely distributed throughout the peripheral and central nervous system, where  
52 they serve as important neuromodulators. Interestingly, unlike other classical  
53 neurotransmitters stored in synaptic vesicles and released from the presynaptic terminal,  
54 eCBs are typically produced and released from the postsynaptic compartment in a  
55 neuronal activity-dependent manner, then retrogradely travel to the presynaptic terminal  
56 and activate the CB1R, activation of which often results in an inhibition of presynaptic  
57 neurotransmitter release<sup>3,4</sup>. In addition, eCBs also play a role in glial cells and in  
58 intracellular organelles<sup>5-9</sup>. In the brain, eCBs participate in the short-term and long-term  
59 synaptic plasticity of glutamatergic and gamma-aminobutyric acid (GABA)-ergic synapses  
60 in a variety of regions, including the cerebral cortex, hippocampus, striatum, ventral  
61 tegmental area, amygdala and cerebellum<sup>4,10</sup>, playing an important role in a wide range of  
62 physiological processes such as development, emotional state, pain, the sleep/wake cycle,  
63 energy metabolism, reward, and learning and memory<sup>11-15</sup>. Given the broad distribution  
64 and variety of functions of eCBs, dysregulation of the eCB system has been associated  
65 with a plethora of disorders, including neuropsychiatric and neurodegenerative diseases,  
66 epilepsy, cancer, and others<sup>16-18</sup>. The eCB system has therefore emerged as a promising  
67 target for treating neurological diseases<sup>19,20</sup>.

68 Although we know much about the eCB biochemistry and physiology, the  
69 spatiotemporal dynamics of eCB release in the brain remains largely unknown. Synaptic  
70 transmission mediated by classic neurotransmitters such as glutamate and GABA and their  
71 respective ionotropic receptors can occur in a timescale on the order of milliseconds and  
72 is generally spatially confined to the synaptic cleft in the nanometer range<sup>21</sup>. In contrast,  
73 signaling via endocannabinoid receptors is believed to last on the order of seconds and  
74 over a distance on the order of tens of microns. However, this assumption has not been  
75 tested directly, largely because existing methods for measuring eCB signaling lack the  
76 necessary spatiotemporal resolution. For example, although qualitative and quantitative  
77 measurement of eCBs in brain tissues can provide valuable information regarding eCB  
78 levels, these measurements usually require the extraction, purification and analysis of  
79 lipids by chromatography and mass spectrometry<sup>22,23</sup>, therefore, this approach has poor  
80 spatial and temporal resolution and cannot be used to measure eCBs *in vivo*. Another  
81 approach is electrophysiology coupled with pharmacology and/or genetics, which is often  
82 used to indirectly measure eCB activity by measuring eCB-mediated synaptic  
83 modulation<sup>24-27</sup>; however, this method is mostly used in *in vitro* preparations and has  
84 relative low spatial resolution. Another method microdialysis, while challenging for  
85 hydrophobic lipid molecules, has been used to monitor eCB abundance in the brain during  
86 pharmacological manipulations and behaviors<sup>28,29</sup>, but it has a long sampling interval (at  
87 least 5 minutes) that is well beyond the time scale of synaptic plasticity mediated by eCBs  
88 (~sub-second to seconds), preventing the accurate detection of eCBs in real time *in vivo*.

89 Therefore, development of an *in vivo* eCB detection tool with satisfactory spatiotemporal  
90 resolution would meet a clear need in this field.

91 Recently, our group and others developed a series of genetically-encoded tools for  
92 sensing neurotransmitters and neuromodulators based on G protein-coupled receptors  
93 (GPCRs) and circular-permuted (cp) fluorescent proteins<sup>30-38</sup>. Using this highly  
94 successful strategy, we developed a novel GPCR activation-based (GRAB) eCB sensor  
95 called GRAB<sub>eCB2.0</sub> (or simply eCB2.0) based on the human CB1R and cpEGFP. The  
96 eCB2.0 sensor has high specificity for eCBs, kinetics on the order seconds, and a  
97 fluorescence response of approximately 800% to 2-AG and 550% to AEA, respectively.  
98 After validating the *in vitro* performance of eCB2.0 in both cultured cells and acute brain  
99 slices, we then expressed the sensor in mice and reliably monitored foot-shock evoked  
100 eCB signals in the basolateral amygdala in freely moving mice and eCB dynamics in the  
101 mouse hippocampus during running and seizure activity.

102

## 103 RESULTS

### 104 Development and *in vitro* characterization of GRAB<sub>eCB</sub> sensors

105 Among the two eCB receptors, we chose CB1R as the scaffold for developing a GRAB  
106 eCB sensor, as this receptor has a higher affinity for eCBs than CB2R<sup>39</sup>. We first inserted  
107 the intracellular loop 3 (ICL3)-cpEGFP module of our recently developed GRAB<sub>NE</sub> sensor<sup>33</sup>  
108 into the corresponding ICL3 in the human CB1R (**Fig. 1a**). After screening various insertion  
109 sites and GRAB<sub>NE</sub> ICL3 truncation constructs, we generated the first-generation eCB  
110 sensor called GRAB<sub>eCB1.0</sub> (eCB1.0), which showed a moderate response (100% increase  
111 in fluorescence) to ligand and an apparent affinity of 3 μM for 2-AG (**Fig. 1b and Extended**  
112 **Data Fig. 1a**). To improve the dynamic range of our eCB sensor, we then selected 8  
113 residues in cpEGFP for individual randomized mutation based on the experience gained  
114 through the development of previous GRAB sensors<sup>30,32-34,36-38</sup> (**Extended Data Fig. 1b**).  
115 Combining several single-mutation candidates—each with improved performance—  
116 resulted in the GRAB<sub>eCB1.5</sub> sensor (eCB1.5), which has a 2-fold higher response than  
117 eCB1.0 (**Extended Data Fig. 1a**). We next focused on the receptor’s ligand binding pocket  
118 in order to further improve the sensor’s dynamic range and affinity. The residues F177<sup>2,64</sup>,  
119 V196<sup>3,32</sup> and S383<sup>7,39</sup> were selected for targeted screening based on the studies of CB1R  
120 structure<sup>40-45</sup> (**Extended Data Fig. 1c**). Interestingly, we found that introducing the  
121 S383<sup>7,39</sup>T mutation in eCB1.5 produced an increased response to 2-AG with a similar  
122 apparent affinity, whereas adding the F177<sup>2,64</sup>A mutation abolished the response to 2-AG  
123 (**Extended Data Fig. 1a**). We therefore selected the eCB1.5 with the S383<sup>7,39</sup>T mutation  
124 as the second-generation GRAB<sub>eCB2.0</sub> sensor (eCB2.0), and eCB1.5 with both the  
125 S383<sup>7,39</sup>T and F177<sup>2,64</sup>A mutations as a non-responsive negative control, which we call  
126 GRAB<sub>eCBmut</sub> sensor (eCBmut) (**Extended Data Fig. 2**).

127 When expressed in HEK293T cells, both the eCB2.0 and eCBmut sensors trafficked  
128 to the cell membrane (**Fig. 1c**). Upon ligand application, eCB2.0 had a concentration-  
129 dependent fluorescence increases to both 2-AG and AEA, with a maximum response of  
130 approximately 2 fold relative to baseline and the half maximal effective concentrations  
131 (EC<sub>50</sub>) for 2-AG and AEA of 7.2 μM and 0.5 μM, respectively; in contrast, eCBmut showed  
132 no response to 2-AG or AEA at all concentrations tested (**Fig. 1d**). We then tested whether

133 the sensor's response is specific to eCBs compared to other neurotransmitters. We found  
134 that eCB2.0 responded robustly to both 10  $\mu$ M AEA and 2-AG, and the response was  
135 abolished by the CB1R inverse agonist AM251; moreover, no other neurotransmitters or  
136 neuromodulators tested elicited a response in cells expressing eCB2.0 (**Fig. 1e**).

137 Next, we measured the kinetics of eCB2.0 signaling using a rapid localized solution  
138 application system in which compounds were puffed directly on the cell (**Fig. 1f**). To  
139 measure the onset rate ( $T_{on}$ ), 100  $\mu$ M 2-AG was puffed on eCB2.0 expressing cell; to  
140 measure the offset rate ( $T_{off}$ ), 100  $\mu$ M AM251 was puffed in the presence of 10  $\mu$ M 2-AG.  
141 Using this approach, we measured averaged  $T_{on}$  and  $T_{off}$  values of 1.6 s and 11.2 s,  
142 respectively (**Fig. 1g**). To examine whether eCB sensors couple with intracellular signaling  
143 pathways, we measured G-protein activation using a  $G_{\beta\gamma}$  bioluminescence resonance  
144 energy transfer (BRET) sensor based on the  $G_{\beta\gamma}$  binding region of phosducin fused to  
145 NanoLuc luciferase. This unified BRET sensor was based upon similar systems<sup>46,47</sup>.  
146 Treating cells expressing CB1R with 2-AG induced a robust increase in BRET, consistent  
147 with G protein activation; in contrast, 2-AG had no effect on BRET in mock-transfected  
148 control cells or in cells expressing either eCB2.0 or eCBmut (**Fig. 1h**). We also measured  
149  $\beta$ -arrestin recruitment using the Tango GPCR assay<sup>48</sup> and found that AEA induced a robust,  
150 concentration-dependent response in cells expressing CB1R but had no effect in control  
151 cells or cells expressing either eCB2.0 or eCBmut (**Fig. 1i**). Taken together, these data  
152 indicate that our eCB2.0 sensor binds eCBs but does not couple to downstream effector  
153 proteins and therefore likely does not affect cellular physiology.

154 We then examined the expression pattern of the eCB sensor in neurons by sparsely  
155 expressing eCB2.0 in cultured rat cortical neurons. We found that eCB2.0 trafficked to the  
156 entire neuronal cell membrane, including the axons and dendrites, as shown by  
157 colocalization with the axonal presynaptic marker synaptophysin-mScarlet and the  
158 postsynaptic marker PSD95-mScarlet (**Fig. 2a**). To measure the response of eCB2.0 in  
159 neurons, we infected cultured rat cortical neurons using an adeno-associated virus (AAV)  
160 expressing either eCB2.0 or eCBmut under the control of the human *SYN1* (synapsin)  
161 promoter to drive expression in all neurons (**Fig. 2b**). We found that both 2-AG and AEA  
162 elicited concentration-dependent fluorescence responses in neurons expressing eCB2.0,  
163 with a maximum fluorescence increase of 800% and 550%, respectively, and an EC<sub>50</sub> value  
164 of 17.2  $\mu$ M and 0.7  $\mu$ M, respectively; in contrast, neither 2-AG nor AEA elicited a response  
165 in neurons expressing eCBmut, even at 100  $\mu$ M (**Fig. 2b,c**). We also found that eCB2.0  
166 responses in neurites were higher than in somata (**Fig. 2d**). Finally, bath application of the  
167 CB1R agonist WIN55212-2—which can activate eCB2.0 in HEK293T cells (**Extended**  
168 **Data Fig. 3a**)—to eCB2.0-expressing neurons induced a fluorescence increase that was  
169 stable for up to 2 hours and blocked completely by AM251 (**Fig. 2e**), suggesting that the  
170 sensor does not undergo arrestin-mediated internalization or desensitization and can be  
171 used for long-term monitoring of eCB activity.

172

### 173 **eCB2.0 can be used to measure endogenous eCBs in primary cultured neurons**

174 Cultured neurons are commonly used for studying eCB mediated synaptic modulation<sup>27,49</sup>.  
175 We therefore examined whether our eCB2.0 sensor can be used to detect the release of  
176 endogenous eCB in cultured rat cortical neurons expressing eCB2.0 together with a red

177 glutamate sensor R<sup>ncp</sup>-iGluSnFR<sup>50</sup>. Applying electrical field stimuli (100 pulses at 50 Hz)  
178 elicited robust eCB and glutamate signals (**Fig. 3a**), demonstrating that eCB2.0 can reliably  
179 report endogenous eCB release and is compatible with red fluorescent indicators. We then  
180 expressed eCB2.0 in neurons loaded with a red fluorescent Ca<sup>2+</sup> dye Calbryte-590 in order  
181 to simultaneously measure eCB release and changes in intracellular Ca<sup>2+</sup>. Applying 100  
182 field stimuli at 50 Hz elicited robust responses with respect to both intracellular Ca<sup>2+</sup> and  
183 eCB release (**Fig. 3b**). Moreover, the rise and decay kinetics of the calcium signal were  
184 faster than those of the eCB signal, consistent with the notion that eCB release requires  
185 neuronal activity<sup>51</sup>. We also found a strong correlation between the peak Ca<sup>2+</sup> signal and  
186 the peak eCB signal when applying increasing numbers of stimuli ( $R^2 = 0.99$ , **Fig. 3c**);  
187 importantly, in the absence of extracellular Ca<sup>2+</sup>, even 20 pulses were unable to elicit either  
188 a Ca<sup>2+</sup> signal or an eCB2.0 response (**Fig. 3c**), confirming the requirement of calcium  
189 activity on eCB release.

190 Next, we asked which specific eCB—2-AG and/or AEA—is released in cultured rat  
191 cortical neurons. 2-AG is mainly produced in neurons from diacylglycerol (DAG) by  
192 diacylglycerol lipase (DAGL), while AEA is mainly produced from *N*-arachidonoyl  
193 phosphatidylethanolamine (NAPE) via the enzyme NAPE-hydrolyzing phospholipase D  
194 (NAPE-PLD) (**Fig. 3d**). We found that the selective DAGL inhibitor DO34<sup>52</sup> eliminated the  
195 stimulus-evoked eCB2.0 signal within 30 min; as a positive control, subsequent application  
196 of the CB1R agonist WIN55212-2 restored eCB2.0 fluorescence, indicating that the sensor  
197 is still present in the cell membrane (**Fig. 3e,f**). We also examined the effect of blocking  
198 the degradation of 2-AG and AEA via the enzymes monoacylglycerol lipase (MAGL) and  
199 fatty acid amide hydrolase (FAAH) using the inhibitors JZL184<sup>53</sup> and URB597<sup>54</sup>,  
200 respectively (**Fig. 3g**). We found that blocking MAGL significantly increased the decay time  
201 constant, while blocking FAAH had only a slight—albeit significant—effect on the decay  
202 time constant. Taken together, these data indicate that 2-AG is the principal eCB released  
203 from cultured rat cortical neurons in response to electrical stimuli.

204 In addition to the stimuli-evoked eCB signals, we also observed local, transient eCB2.0  
205 signals in neurons that occurred spontaneously in the absence of external stimulation (**Fig.**  
206 **3j**). The peak amplitude and rise kinetics of these transient eCB2.0 signals were smaller  
207 and slower compared to the signal measured in response to a single electrical stimulus  
208 recording in the same region of interest (ROI) (**Fig. 3k,l**), suggesting that evoked and  
209 spontaneous eCB release have distinct patterns. The average diameter of the  
210 spontaneous transient signals was 11.3 μm based on our analysis of full width at half  
211 maximum (FWHM) (**Fig. 3m**), consistent with previous suggestions that eCB acts  
212 locally<sup>55,56</sup>. Finally, the CB1R inverse agonist AM251 eliminated the spontaneous transient  
213 eCB2.0 signals (**Fig. 3l,n,o**).

214

### 215 **eCB2.0 can be used to measure eCB release in acute mouse brain slices**

216 Next, we examined whether our eCB sensor can be used to detect endogenous eCB  
217 release in a more physiologically relevant system, namely acute mouse brain slices. We  
218 first injected AAVs expressing either eCB2.0 or eCBmut into the dorsolateral striatum (DLS)  
219 of adult mice (**Fig. 4a**), the region where eCB mediates both short-term and long-term  
220 depression and regulates motor behavior<sup>57-59</sup>. Four weeks after AAV injection, acute brain

221 slices were prepared, showing the expression of eCB sensors in DLS (**Fig. 4b**). The  
222 fluorescence signals evoked by electrical stimuli in the DLS were recorded by photometry.  
223 We found that applying electrical stimuli in eCB2.0-expressing slices evoked clear  
224 fluorescence signals, with stronger responses evoked by increasing the number of stimuli  
225 and by increasing the stimulation frequency (**Fig. 4c,d**). The half-rise time and decay time  
226 constant ranged from 0.8–1.2 s and 5.2–8.5 s, respectively, depending on the number of  
227 pulses and the stimulation frequency (**Fig. 4d**). Moreover, the signal was specific to eCB  
228 release, as pretreating the slices with 10  $\mu$ M AM251 blocked the response, and no  
229 response was measured in slices expressing the eCBmut mutant sensor (**Fig. 4e**). In a  
230 separate experiment, the expression of eCB2.0 in neurites in a striatal slice was detected  
231 by 2-photon (2P) fluorescence microscopy; applying AEA induced an increase of eCB2.0  
232 fluorescence that was reversed by AM251 (**Extended Data Fig. 4**).

233 We also expressed the eCB2.0 in the hippocampal CA1 region (**Fig. 4f**), in which eCB  
234 modulates both excitatory and inhibitory inputs<sup>60,61</sup>, and then recorded eCB2.0 signals in  
235 acute slices using 2P microscopy. Consistent with our results measured in the DLS, we  
236 found that applying an increasing number of electrical stimuli at 20 Hz evoked increasingly  
237 larger changes in eCB2.0 fluorescence (**Fig. 4g,h**). In addition, applying 10  $\mu$ M AEA to the  
238 slices caused a large increase in eCB2.0 fluorescence that was reversed by 10  $\mu$ M AM251  
239 (**Fig. 4i**). Finally, AM251 eliminated the signal induced by even 100 field stimuli (**Fig. 4j**).  
240 These *in vitro* data confirm that eCB2.0 can be used to reliably detect the endogenous  
241 release of eCBs in acute brain slices with high sensitivity, specificity, and spatiotemporal  
242 resolution.

243

#### 244 **eCB2.0 can be used to measure foot shock-induced eCB release in the basolateral 245 amygdala of freely moving mice**

246 The basolateral amygdala (BLA) is a key brain region mediating fear responses and  
247 processing aversive memories<sup>62</sup>. Previous studies found that the CB1R is highly expressed  
248 in the BLA, and the eCB system in BLA participates in stress expression<sup>63–65</sup>. We therefore  
249 tested whether our eCB2.0 sensor could be used to directly measure eCB dynamics *in vivo*  
250 while applying an aversive stimulus (foot shock); for these experiments, we injected AAV  
251 vectors expressing either eCB2.0 or eCBmut together with AAVs expressing the mCherry  
252 in the mouse BLA and then performed fiber photometry recording (**Fig. 5a,b**). We found  
253 that applying a 2-sec foot shock induced a time-locked transient increase in eCB2.0  
254 fluorescence in the BLA (**Fig. 5c**); this response was highly reproducible over 5  
255 consecutive trials (**Fig. 5d**). Importantly, the same foot shock had no effect on either  
256 mCherry fluorescence or eCBmut fluorescence (**Fig. 5c,e**). The average time constant for  
257 the rise and decay phases of the eCB2.0 signal was 1.0 s and 6.3 s, respectively (**Fig. 5f**).  
258 These data indicate that eCB2.0 can be used to measure eCB dynamics *in vivo* in freely  
259 moving animals.

260

#### 261 **Dual-color imaging of eCB2.0 and a genetically encoded Ca<sup>2+</sup> indicator expressed in 262 the mouse hippocampal CA1 region measured during running and seizure activity**

263 Our finding that eCB2.0 can be expressed in the mouse hippocampal CA1 region and then  
264 measured in acute slices led us to ask whether we could use this sensor to measure *in*

265 *vivo* eCB dynamics in the CA1 region during physiologically relevant activity such as  
266 running. We therefore injected AAVs expressing eCB2.0 or eCBmut together with a red  
267 Ca<sup>2+</sup> indicator jRGECO1a<sup>66</sup> into mouse hippocampal CA1 region and then conducted  
268 head-fixed 2P dual-color imaging through an implanted cannula above the hippocampus  
269 (**Fig. 6a**). Co-expression of eCB2.0 and jRGECO1a was clearly observed in neurons in the  
270 CA1 4–6 weeks after virus injection (**Fig. 6b**). We focused on the *stratum pyramidale* layer,  
271 which is composed of pyramidal neuron somata and interneuron axons, including a class  
272 that densely express CB1R. When mice spontaneously ran on a treadmill (**Fig. 6c**), we  
273 found rapid increases of both calcium and eCB signals aligned to the start of running, and  
274 decreases of both signals when the running stopped (**Fig. 6d,e**). In the control group, which  
275 expressed eCBmut and jRGECO1a, calcium signals were intact while eCBmut showed no  
276 fluorescence change (**Fig. 6d,e**). Interestingly, the calcium signal appeared earlier than the  
277 eCB signal, although both signals had similar 10%-90% rise time, while the half-time of the  
278 decay phase of eCB signal was slower than that of the calcium signal (**Fig. 6f**).

279 Epilepsy is a neurological disease characterized by excessive and synchronous  
280 neuronal firing. eCBs are proposed to provide negative feedback during epilepsy to  
281 attenuate the synaptic activity and protect the nervous system, which is exemplified by the  
282 observation that animals with compromised eCB system all exhibit a pro-epileptic  
283 phenotype<sup>67</sup>. To explore whether our eCB2.0 sensor could be used to study seizure-related  
284 eCB signals *in vivo*, we used electrical kindling stimulation of the hippocampus  
285 contralateral to the sensor expressing hemisphere to elicit brief self-terminating seizures  
286 (measured using local field potential (LFP) recording) (**Fig. 6g**). We found strong calcium  
287 and eCB signal increases during electrical seizure activity (**Fig. 6h**). Recent work has  
288 shown that seizures are often followed by a spreading calcium wave that propagates  
289 across the cell layer<sup>68</sup>. Interestingly, we also found a propagating eCB wave that closely  
290 followed the calcium wave (**Fig. 6h, Extended Data Fig.5 and Supplementary Video 1**).  
291 In contrast, eCBmut showed no response during and after seizures (**Fig. 6i**). The velocity  
292 and direction of eCB waves were evident when we extracted the eCB2.0 signal from  
293 individual neurons in the field of view (**Fig. 6j,k**). Notably, eCB waves and calcium waves  
294 varied across experiment sessions and animals (**Fig. 6l**), but for each instance, the calcium  
295 and eCB waves were similar, in agreement with the calcium- and activity-dependence of  
296 the eCB signal. Taken together, our results confirm that the eCB2.0 sensor can be used to  
297 measure eCB dynamics *in vivo* under both physiological and pathological conditions, with  
298 high specificity and spatiotemporal resolution.  
299

## 300 DISCUSSION

301 Here, we report the development and characterization of a genetically-encoded fluorescent  
302 sensor for detecting eCBs both *in vitro* and *in vivo*. With high sensitivity, selectivity and  
303 kinetics, this novel eCB sensor can be used to detect endogenous eCB release in cultured  
304 neurons, acute brain slices and in specific brain structures *in vivo* such as the amygdala  
305 and hippocampus during both physiological and pathological activities.

306 Our estimate of  $T_{on}$  and  $T_{off}$  kinetics measured for eCB2.0 in cultured neurons at room  
307 temperature is likely high, given that a faster time constant was measured in acute slices  
308 and in our *in vivo* experiments. Nevertheless, given that the temporal resolution of eCB2.0

309 is on the order of seconds, this tool is a vast improvement compared to microdialysis (with  
310 temporal resolution on the order of minutes), although the sensor's kinetics could be  
311 improved even further in order to capture more rapid signals<sup>69</sup>. In addition, the eCB2.0  
312 sensor can detect both 2-AG and AEA; given that 2-AG and AEA regulate distinct pathways  
313 and are involved in different brain regions and cell types<sup>4</sup>, next-generation GRAB<sub>eCB</sub>  
314 sensors should be developed with non-overlapping eCB specificity, as well as non-  
315 overlapping color spectra.

316 The retrograde modulation of synaptic activity by eCBs was previously identified by  
317 studying depolarization-induced suppression of inhibition (DSI) and excitation (DSE) in the  
318 hippocampus and cerebellum<sup>24,25,27</sup>. However, because these experiments and  
319 subsequent studies used electrophysiological recordings of synaptic transmission  
320 combined with either pharmacological interventions (e.g., to activate or inhibit eCB  
321 receptors or to inhibit enzymes involved in the production or degradation of eCBs) or  
322 genetic manipulation (e.g., by knocking out the corresponding receptors and enzymes),  
323 they lacked the ability to directly measure eCB release. Moreover, recording at the cell  
324 body of a neuron does not provide precise spatial information with respect to eCB release.  
325 For example, DSI recorded using paired whole-cell recordings in hippocampal slices  
326 indicates that depolarization of one neuron can inhibit GABAergic input to neurons within  
327 approximately 20 μm, suggesting the upper limit of diffusion for eCBs from a single  
328 neuron<sup>24</sup>; similar results were obtained in cerebellar slices using two separate stimulating  
329 electrodes to evoke eCB release from two dendritic regions in a single Purkinje cell<sup>55</sup>.  
330 Although these data indicate that eCB signaling is relatively localized and tightly controlled,  
331 the detailed spatial profile of eCB signaling is unknown. In addition, although the sampling  
332 rate of electrophysiological recordings is generally high (e.g., on the order of several kHz),  
333 the eCB signals measured by changes in evoked postsynaptic currents (ePSCs) have a  
334 sampling interval of approximately 2 s, creating a temporal bottleneck. In this respect, our  
335 eCB2.0 sensor can reveal eCB signals with considerably higher spatial and temporal  
336 resolution, similar to recent studies using sensors for detecting other neurotransmitters<sup>70,71</sup>.  
337 Using cultured neurons, we found that spontaneous eCB transients are confined to an area  
338 with a diameter of approximately 11 μm, smaller than previous estimates of eCB diffusion.  
339 In the future, it will be interesting to determine whether these local transient signals  
340 originate from single spines.

341 In summary, we show that our eCB2.0 sensor can be used in a variety of *in vitro* and  
342 *in vivo* preparations in order to monitor eCB dynamics in real time. Given the complexity of  
343 the nervous system, future directions for research based on the eCB sensor applications  
344 may include the identity of cell types that release eCBs, the mechanisms and temporal  
345 properties of eCB release, characteristics of eCB diffusion, the duration of eCB signals, the  
346 nature of the cell types and subcellular elements targeted by eCBs and the effects on them.  
347 Answering these fundamental questions will significantly enrich our understanding of the  
348 mechanisms and functions of eCB signaling at the synapse and neural circuit levels. Lastly,  
349 altered function of the eCB system has been associated with several neurological disorders,  
350 including stress/anxiety, movement disorders, substance use disorders and epilepsy. In  
351 this respect, our *in vivo* results show clear examples of how the eCB2.0 sensor could help  
352 to elucidate the fast eCB dynamics during both physiological and pathological processes.

353 The eCB2.0 sensor should be able to detect all CB1R agonists (**Extended Data Fig. 3**)  
354 including Δ-9-tetrahydrocannabinol (Δ-9-THC) in the brain and periphery following drug  
355 administration. This would also allow investigators to track the time course of Δ-9-THC  
356 actions and the impact of cannabis drugs on eCB signaling. Thus, eCB sensors open a  
357 new era of endocannabinoid research aimed at understanding this system at  
358 unprecedented, physiologically-relevant spatial and temporal scales.  
359

360 **METHODS**

361 **Molecular biology**

362 DNA fragments were amplified by PCR using primers (TSINGKE Biological Technology)  
363 with 25–30-bp overlaps. Plasmids were constructed using restriction enzyme cloning or  
364 Gibson Assembly, and all plasmid sequences were verified using Sanger sequencing. To  
365 characterize eCB2.0 and eCBmut in HEK293T cells, the corresponding DNA constructs  
366 were cloned into the pDisplay vector with an upstream IgK leader sequence. An IRES-  
367 mCherry-CAAX cassette was inserted downstream of the sensor gene for labeling the cell  
368 membrane and calibrating the sensor's fluorescence. To characterize eCB2.0 in neurons,  
369 the eCB2.0 was cloned into a pAAV vector under control of a human synapsin (*SYN1*)  
370 promoter (pAAV-hSyn), and PSD95-mScarlet and synaptophysin-mScarlet were cloned  
371 into the pDest vector under the control of the *CMV* promoter. For the  $G_{\beta\gamma}$  sensor assay, the  
372 human CB1R was cloned into the pCI vector (Promega), and eCB2.0 and eCBmut were  
373 cloned into the peGFP-C1 vector (Takara), replacing the eGFP open reading frame. For  
374 the Tango assay, the human CB1R, eCB2.0 and eCBmut were cloned into the pTango  
375 vector. In addition, the viral vectors pAAV-hsyn-eCBmut and pAAV-hsyn-R<sup>ncp</sup>-iGluSnFR  
376 were generated and used in this study.

377

378 **AAV expression**

379 AAV2/9-hSyn-eCB2.0 ( $9.5 \times 10^{13}$  viral genomes (vg)/mL), AAV2/9-hSyn-eCBmut ( $8.0 \times 10^{13}$   
380 vg/mL), AAV2/9-hSyn-R<sup>ncp</sup>-iGluSnFR ( $6.2 \times 10^{13}$  vg/mL, all packaged at Vigene  
381 Biosciences, China), AAV8-hSyn-mCherry (#114472, Addgene) and AAV1-Syn-NES-  
382 jRGECO1a-WPRE-SV40 (Penn Vector Core) were used to infect cultured neurons or were  
383 injected *in vivo* into specific brain regions.

384

385 **Cell culture**

386 HEK293T cells were cultured at 37°C in air containing 5% CO<sub>2</sub> in DMEM (Biological  
387 Industries) supplemented with 10% (v/v) fetal bovine serum (Gibco) and penicillin (100  
388 unit/mL)-streptomycin (0.1 mg/mL) (Biological Industries). For experiments, the HEK293T  
389 cells were plated on 96-well plates or 12 mm glass coverslips in 24-well plates. At 60–70%  
390 confluence, the cells were transfected using polyethylenimine (PEI) with 300 ng DNA/well  
391 (for 96-well plates) or 1  $\mu$ g DNA/well (for 24-well plates) at a DNA:PEI ratio of 1:3; 4–6 h  
392 after transfection, the culture medium was replaced with fresh medium. Imaging was  
393 performed 24–36 h after transfection. Rat cortical neurons were prepared from postnatal  
394 day 0 (P0) Sprague-Dawley rat. In brief, the cerebral cortex was dissected, and cortical  
395 neurons were dissociated by digestion in 0.25% Trypsin-EDTA (Biological Industries), and  
396 then plated on poly-D-lysine-coated (Sigma-Aldrich) 12-mm glass coverslips in 24-well  
397 plates. The neurons were cultured at 37°C, 5% CO<sub>2</sub> in Neurobasal Medium (Gibco)  
398 supplemented with 2% B-27 Supplement (Gibco), 1% GlutaMAX (Gibco), and penicillin  
399 (100 unit/mL)-streptomycin (0.1 mg/mL) (Biological Industries). For transfection, cultured  
400 neurons were transfected at 7–9 day *in vitro* (DIV7–9) using calcium phosphate  
401 transfection method and imaged 48 h after transfection. For viral infection, cultured  
402 neurons were infected by AAVs expressing eCB2.0, eCBmut and/or R<sup>ncp</sup>-iGluSnFR at  
403 DIV3–5 and imaged at DIV12–20. Where indicated, the neurons were loaded with

404 Calbryte-590 (AAT Bioquest) 1 h before imaging.

405

## 406 **Animals**

407 All experiment protocols were approved by the respective Laboratory Animal Care and Use  
408 Committees of Peking University, the National Institute on Alcohol Abuse and Alcoholism,  
409 the Cold Spring Harbor Laboratory, and Stanford University, and all studies were performed  
410 in accordance with the guidelines established by the US National Institutes of Health.  
411 Postnatal day 0 (P0) Sprague-Dawley rats (Beijing Vital River Laboratory) of both sexes  
412 and P42–P150 C57BL/6J mice (Beijing Vital River Laboratory and The Jackson Laboratory)  
413 of both sexes were used in this study. The mice were housed under a normal 12-h light/dark  
414 cycle with food and water available *ad libitum*.

415

## 416 **Confocal imaging of cultured cells**

417 Before imaging, the culture medium was replaced with Tyrode's solution consisting of (in  
418 mM): 150 NaCl, 4 KCl, 2 MgCl<sub>2</sub>, 2 CaCl<sub>2</sub>, 10 HEPES, and 10 glucose (pH 7.4). 0 mM  
419 [Ca<sup>2+</sup>]<sub>ex</sub> solution was modified from Tyrode's solution with 0 mM CaCl<sub>2</sub> and additional 2 mM  
420 EGTA. HEK293T cells in 96-well plates were imaged using an Opera Phenix high-content  
421 screening system (PerkinElmer, USA) equipped with a 20x/0.4 NA objective, a 40x/0.6 NA  
422 objective, a 40x/1.15 NA water-immersion objective, a 488 nm laser and a 561 nm laser.  
423 Green and red fluorescence were collected using a 525/50 nm emission filter and a 600/30  
424 nm emission filter, respectively. Cells in 12 mm coverslips were imaged using a Ti-E A1  
425 confocal microscopy (Nikon, Japan) equipped with a 10x/0.45 NA objective, a 20x/0.75 NA  
426 objective, a 40x/1.35 NA oil-immersion objective, a 488 nm laser and a 561 nm laser. Green  
427 and red fluorescence were collected using a 525/50 nm emission filter and a 595/50 nm  
428 emission filter, respectively. The following compounds were applied by replacing the  
429 Tyrode's solution (for imaging in 96-well plates) or by either bath application or using a  
430 custom-made perfusion system (for imaging cells on 12-mm coverslips): 2-AG (Tocris),  
431 AEA (Cayman), AM251 (Tocris), LPA (Tocris), S1P (Tocris), ACh (Solarbio), DA (Sigma-  
432 Aldrich), GABA (Tocris), Glu (Sigma-Aldrich), Gly (Sigma-Aldrich), NE (Tocris), 5-HT  
433 (Tocris), His (Tocris), Epi (Sigma-Aldrich), Ado (Tocris), Tyr (Sigma-Aldrich), WIN55212-2  
434 (Cayman), DO34 (MedChemExpress), JZL184 (Cayman), and URB597 (Cayman). The  
435 micropressure application of drugs was controlled by Pneumatic PicoPump PV800 (World  
436 Precision Instruments). Cultured neurons were field stimulated using parallel platinum  
437 electrodes positioned 1 cm apart; the electrodes were controlled by a Grass S88 stimulator  
438 (Grass Instruments), and 1-ms pulses were applied at 80 V. All imaging experiments were  
439 performed at room temperature (22–24°C).

440

## 441 **BRET G<sub>βγ</sub> sensor assay**

442 Plasmids expressing eCB2.0, eCBmut, or CB1R were co-transfected into HEK293T cells  
443 together with a single construct expressing human GNAOa, human GNB1 (fused to amino  
444 acids 156–239 of Venus), human GNG2 (fused to amino acids 2–155 of Venus), and  
445 NanoLuc fused to the amino terminal 112 amino acids of human Phosducin circularly  
446 permuted at amino acids 54/55 (Promega). The NanoLuc/Phosducin fusion portion also  
447 contains a kRAS membrane targeting sequence at the carboxy terminal end. Templates

448 for assembly were derived from human whole-brain cDNA (Takara) for all cDNAs, except  
449 for the hGNB1 and hGNG2 Venus fusions which were a generous gift from Dr. Nevin  
450 Lambert (Augusta University). Approximately 24 hours after transfection, the cells were  
451 harvested with 10 mM EDTA in phosphate-buffered saline (PBS, pH 7.2), pelleted, and  
452 then resuspended in Dulbecco's modified PBS (Life Technologies) without Ca<sup>2+</sup> or Mg<sup>2+</sup>.  
453 Furimazine (Promega) was then added at a 1/100 dilution to 100 µl of cell suspension in a  
454 black 96-well plate, and BRET was measured using a PHERAstar FS plate reader  
455 (Berthold) equipped with a Venus BRET cube. The acceptor (Venus) and donor (NanoLuc)  
456 signals were measured at 535 nm and 475 nm, respectively, and net BRET was calculated  
457 by subtracting the acceptor/donor ratio of a donor-only sample from the acceptor/donor  
458 ratio of each sample. Readings were taken before and 3–4 min after application of 20 µM  
459 2-AG (Tocris) to activate CB1R or the eCB sensor.  
460

#### 461 **Tango assay**

462 Plasmids expressing eCB2.0, eCBmut, or CB1R were transfected into a reporter cell line  
463 expressing a β-arrestin2-TEV fusion gene and a tTA-dependent luciferase reporter gene.  
464 24 h after transfection, cells in 6 well plates were collected after trypsin digestion and plated  
465 in 96 well plates. AEA was applied at final concentrations ranging from 0.01 nM to 10 µM.  
466 12 h after luciferase expression, Bright-Glo (Fluc Luciferase Assay System, Promega) was  
467 added to a final concentration of 5 µM, and luminescence was measured using the VICTOR  
468 X5 multi-label plate reader (PerkinElmer).  
469

#### 470 **Photometry recording in the dorsolateral striatum in acute mouse brain slices**

471 Adult (>10 weeks of age) male C57BL/6J mice were anesthetized with isoflurane, AAV  
472 vectors were injected (300 nl at a rate of 50 nl/min) into the dorsolateral striatum at the  
473 following coordinates: A/P: +0.75 mm relative to Bregma; M/L: ±2.5 mm relative to Bregma;  
474 and D/V: -3.5 mm). After virus injection, the mice received an injection of ketoprofen (5  
475 mg/kg, s.c.), and postoperative care was provided daily until the mice regained their  
476 preoperative weight. After a minimum of 4 weeks following AAV injection, the mice were  
477 deeply anesthetized with isoflurane, decapitated, and the brains were removed and placed  
478 in ice-cold cutting solution containing (in mM): 194 sucrose, 30 NaCl, 4.5 KCl, 26 NaHCO<sub>3</sub>,  
479 1.2 NaH<sub>2</sub>PO<sub>4</sub>, 10 D-glucose, and 1 MgCl<sub>2</sub> saturated with 5% CO<sub>2</sub>/95% O<sub>2</sub>. Coronal brain  
480 slices (250-µm thickness) were prepared and then incubated at 32°C for 60 min in artificial  
481 cerebrospinal fluid (ACSF) containing (in mM): 124 NaCl, 4.5 KCl, 26 NaHCO<sub>3</sub>, 1.2  
482 NaH<sub>2</sub>PO<sub>4</sub>, 10 D-glucose, 1 MgCl<sub>2</sub>, and 2 CaCl<sub>2</sub>. After incubation at 32°C, the slices were  
483 kept at room temperature until use. Photometry recordings were acquired using an  
484 Olympus BX41 upright epifluorescence microscope equipped with a 40x/0.8 NA water-  
485 emersion objective and a FITC filter set. Slices were superfused at 2 ml/min with ACSF  
486 (29–31°C). A twisted bipolar polyimide-coated stainless-steel stimulating electrode (~200  
487 µm tip separation) was placed in the DLS just medial to the corpus callosum and slightly  
488 below the tissue surface in a region with visible eCB2.0 or eCBmut fluorescence. The  
489 sensors were excited using either a 470-nm light-emitting diode (LED) (ThorLabs). Photons  
490 passing through a 180-µm<sup>2</sup> aperture positioned just lateral to the stimulating electrode were  
491 directed to a model D-104 photomultiplier tube (PMT) (Photon Technology International).

492 The PMT output was amplified (gain: 0.1  $\mu$ A/V; time constant: 5 ms), filtered at 50 Hz, and  
493 digitized at 250 Hz using a Digidata 1550B and Clampex software (Molecular Devices).  
494 For each photometry experiment, GRAB<sub>eCB</sub> was measured as discrete trials repeated  
495 every 3 minutes. For each trial, the light exposure duration was 35–45 seconds in order to  
496 minimize GRAB<sub>eCB</sub> photobleaching while capturing the peak response and the majority of  
497 the decay phase. To evoke an eCB transient, a train of 200–500- $\mu$ s electrical pulses (1.0–  
498 1.5 mA) was delivered 5 s after initiating GRAB<sub>eCB</sub> excitation.  
499

500 **2-photon imaging in the hippocampus in acute mouse brain slices**

501 Adult (6–8 weeks of age) C57BL/6J mice of both sexes were anesthetized with an  
502 intraperitoneal injection of 2,2,2-tribromoethanol (Avertin, 500 mg/kg body weight, Sigma-  
503 Aldrich), and AAV vectors were injected (400 nl at a rate of 46 nl/min) into the hippocampal  
504 CA1 region using the following coordinates: A/P: −1.8 mm relative to Bregma; M/L: ±1.0  
505 mm relative to Bregma; and D/V: −1.2 mm. After at least 4 weeks following AAV injection,  
506 the mice were deeply anesthetized with an intraperitoneal injection of 2,2,2-  
507 tribromoethanol, decapitated, and the brains were removed and placed in ice-cold cutting  
508 solution containing (in mM): 110 choline-Cl, 2.5 KCl, 0.5 CaCl<sub>2</sub>, 7 MgCl<sub>2</sub>, 1 NaH<sub>2</sub>PO<sub>4</sub>, 1.3  
509 Na ascorbate, 0.6 Na pyruvate, 25 NaHCO<sub>3</sub>, and 25 glucose saturated with 5% CO<sub>2</sub>/95%  
510 O<sub>2</sub>. Coronal brain slices (300- $\mu$ m thickness) were prepared and incubated at 34°C for  
511 approximately 40 min in modified ACSF containing (in mM): 125 NaCl, 2.5 KCl, 2 CaCl<sub>2</sub>,  
512 1.3 MgCl<sub>2</sub>, 1 NaH<sub>2</sub>PO<sub>4</sub>, 1.3 Na ascorbate, 0.6 Na pyruvate, 25 NaHCO<sub>3</sub>, and 25 glucose  
513 saturated with 5% CO<sub>2</sub>/95% O<sub>2</sub>. Two-photon imaging were performed using an  
514 FV1000MPE 2-photon microscope (Olympus) equipped with a 25x/1.05 NA water-  
515 immersion objective and a mode-locked Mai Tai Ti:Sapphire laser (Spectra-Physics). The  
516 slices were superfused with modified ACSF (32–34°C) at a rate of 4 ml/min. A 920-nm laser  
517 was used to excite the eCB2.0 sensor, and fluorescence was collected using a 495–540-  
518 nm filter. For electrical stimulation, a bipolar electrode (cat. number WE30031.0A3,  
519 MicroProbes for Life Science) was positioned near the stratum radiatum layer in the CA1  
520 region using fluorescence guidance. Fluorescence imaging and electrical stimulation were  
521 synchronized using an Arduino board with custom-written software. All images collected  
522 during electrical stimulation were recorded at a frame rate of 2.8 fps with a frame size of  
523 256×192 pixels. The stimulation voltage was 4–6 V, and the pulse duration was 1 ms.  
524 Drugs were applied to the imaging chamber by perfusion at a flow rate at 4 ml/min.  
525

526 **Fiber photometry recording of eCB signals in the basolateral amygdala**

527 Adult (10–12 weeks of age) C57BL/6J mice of both sexes anesthetized, and 300 nl of  
528 either a 10:1 mixture of AAV-hSyn-eCB2.0 and AAV-hSyn-mCherry or a 10:1 mixture of  
529 AAV-hSyn-eCBmut and AAV-hSyn-mCherry was injected using a glass pipette and a  
530 Picospritzer III microinjection system (Parker Hannifin) into the right basolateral amygdala  
531 using the following coordinates: A/P: −1.78 mm relative to Bregma; M/L −3.30 mm relative  
532 to Bregma; and D/V: −4.53 mm. After injection, a 200- $\mu$ m diameter, 0.37 NA fiber (Inper)  
533 was implanted at the same location and secured using resin cement (3M). A head bar was  
534 also mounted to the skull using resin cement. At least 14 days after surgery, photometry  
535 recording was performed using a commercial photometry system (Neurophotometrics). A

536 patch cord (0.37 NA, Doric Lenses) was attached to the photometry system and to the fiber  
537 secured in the mouse brain. A 470-nm LED was used to excite the GRAB<sub>eCB</sub> sensors, and  
538 a 560-nm LED was used to excite mCherry. The average power level of the LED (measured  
539 at the output end of the patch cord) was 160 µW and 25 µW for the GRAB<sub>eCB</sub> sensors and  
540 mCherry, respectively. The recording frequency was 10 Hz, and the photometry data were  
541 acquired using Bonsai 2.3.1 software.

542 For the foot shock experiments, the mice were allowed to move freely in a Habitest  
543 shock box (Coulbourn Instruments) inside a lighted soundproof behavior box. The  
544 FreezeFrame software program was used to apply triggers to the shock generator  
545 (Coulbourn Instruments). Five 2-sec pulses of electricity at an intensity of 0.7 mA were  
546 delivered to the shock box, with an interval of 90–120 s between trials. After photometry  
547 recording, the animals were deeply anesthetized and perfused with PBS followed by 4%  
548 paraformaldehyde (PFA) in PBS. The brains were removed, fixed in 4% PFA overnight,  
549 and then dehydrated with 30% sucrose in PBS for 24 h. Brain slices were cut using a Leica  
550 SM2010R microtome (Leica Biosystems). Floating brain slices were blocked at room  
551 temperature for 2 h with a blocking solution containing 5% (w/v) BSA and 0.1% Triton X-  
552 100 in PBS, and then incubated at 4°C for 24 h in PBS containing 3% BSA, 0.1% Triton X-  
553 100, and the following primary antibodies: chicken anti-GFP (1:1000, Aves, #GFP-1020)  
554 and rabbit anti-RFP (1:500, Rockland, #600-401-379). The next day, the slices were rinsed  
555 3 times in PBS and incubated in PBS with DAPI (5 µg/ml, Invitrogen, #D1306) and the  
556 following secondary antibodies at 4°C for 24 h: Alexa Fluor 488 donkey anti-chicken (1:250,  
557 Jackson ImmunoResearch, #703-545-155) and Alexa Fluor 568 donkey anti-rabbit (1:250,  
558 Invitrogen, #A10042). Confocal images were captured using an LSM780 confocal  
559 microscope (Zeiss).

560

## 561 **2-photon *in vivo* imaging**

562 Adult (100–150 days of age) C57BL/6J mice of both sexes were used for these  
563 experiments. The mice were anesthetized, and a mixture of AAV1-Syn-NES-jRGECO1a-  
564 WPRE-SV40 and either AAV9-hSyn-eCB2.0 or AAV9-hSyn-eCBmut (300–400 nl each, full  
565 titer) was injected into the right hippocampal CA1 region at the following coordinates using  
566 a Hamilton syringe: A/P: 2.3 mm relative to Bregma; M/L: 1.5 mm relative to Bregma; and  
567 D/V: –1.35 mm. After virus injection, a stainless-steel cannula with an attached coverglass  
568 was implanted over the hippocampus as described previously<sup>72,73</sup>, and a stainless-steel  
569 head bar was attached. A chronic bipolar wire electrode (tungsten, 0.002", 0.5-mm tip  
570 separation, A-M Systems) was implanted into the left ventral hippocampus at the following  
571 coordinates as previously described<sup>74</sup>: A/P: 3.2 mm relative to Bregma; M/L: 2.7 mm  
572 relative to Bregma; and D/V: –4.0 mm. Head-fixed mice running on a linear treadmill with  
573 a 2-m-long cue-less belt were imaged using a resonant scanning 2-photon microscope  
574 (Neurolabware) equipped with a pulsed IR laser tunned to 1000 nm (Mai Tai, Spectra-  
575 Physics), GaAsP PMT detectors (H11706P-40, Hamamatsu), and a 16x/0.8 NA water-  
576 immersion objective (Nikon). The 2-photon image acquisition and treadmill speed were  
577 controlled and monitored using a Scanbox (Neurolabware). Bipolar electrodes were  
578 recorded using a model 1700 differential amplifier (A-M Systems). Seizures were elicited  
579 by applying an electric stimulation above the seizure threshold by 150 µA of current

580 delivered in 1-ms biphasic pulses at 60 Hz for 1 s, using a model 2100 constant-current  
581 stimulator (A-M Systems). Following the *in vivo* recordings, the mice were anesthetized  
582 with isoflurane followed by an intraperitoneal injection of a mixture of ketamine (100 mg/kg  
583 body weight) and xylazine (10 mg/kg body weight) in saline. The mice were transcardially  
584 perfused with 0.9% NaCl for 1 min followed by 4% PFA and 0.2% picric acid in 0.1 M  
585 phosphate buffer. The brains were removed, post-fixed in the same fixative solution for 24  
586 h at 4°C, then sliced on a VTS1200 vibratome (Leica Biosystems). The sections were then  
587 washed and mounted using VECTASHIELD (Vector Laboratories). Confocal images were  
588 acquired using an LSM710 imaging system equipped with a 20x/0.8 NA objective (Zeiss).  
589

590 **Data processing**

591 *Confocal imaging*

592 Data for 96-well plate imaging were collected and analyzed using Harmony high-content  
593 imaging and analysis software (PerkinElmer). In brief, membrane regions were selected  
594 as regions of interest (ROIs) and the green fluorescence channel (i.e., the sensor) was  
595 normalized to the red fluorescence channel corresponding to mCherry-CAAX (G/R).  $\Delta F/F_0$   
596 was then calculated using the formula  $[(G/R_{\text{drug}} - G/R_{\text{baseline}})/(G/R_{\text{baseline}})]$ . For 12-mm  
597 coverslip imaging, data were collected using the NIS-Element software (Nikon) and  
598 analyzed using ImageJ software (National Institutes of Health).  $\Delta F/F_0$  was calculated as  
599 using the formula  $[(F_t - F_0)/F_0]$ , with  $F_0$  representing baseline fluorescence. Data were  
600 plotted using OriginPro 2020 (OriginLab).

601

602 *Slice photometry and 2-photon imaging*

603 For slice photometry, GRAB<sub>ECB</sub> signals were calculated as  $\Delta F/F_0$  by averaging the PMT  
604 voltage (V) for a period of 1 s just prior to electrical stimulation ( $F_0$ ) and then calculating  
605  $[V/(F_0-1)]$  for each digitized data sample. The decay phase was fitted with a single  
606 exponential, accounting for a sloping baseline. Rise  $t_{1/2}$  was calculated in Prism v.  
607 8.3(GraphPad) by fitting the rising phase of the signal with an asymmetrical logistics curve.  
608 Photometry sweeps were exported to Microsoft Excel 2016 to calculate normalized  $\Delta F/F_0$   
609 traces and peak  $\Delta F/F_0$  values. For 2-photon imaging of slices, data were collected using  
610 FV10-ASW software (Olympus) and analyzed using ImageJ.  $\Delta F/F_0$  was calculated using  
611 the formula  $[(F_t - F_0)/F_0]$ , with  $F_0$  representing baseline fluorescence. Data were plotted  
612 using OriginPro 2020.

613

614 *Fiber photometry in mice during foot shock*

615 The fiber photometry data were analyzed off-line using MatLab software (MathWorks) and  
616 plotted using OriginPro 2020.

617

618 *2-photon imaging in mice during locomotion and seizure*

619 Imaging data were processed and analyzed using Python scripts. To analyze single-cell  
620 responses, movies were initially motion-corrected using rigid translation, followed by non-  
621 rigid correction (*HiddenMarkov2D*) using the sima package<sup>75</sup>. Binary ROIs were selected  
622 using a semi-automated approach. For the initial automated detection, movies were  
623 divided into segments consisting of 100 frames each; the average intensity projection of

624 each segment was then computed, and the resulting resampled movie was used for  
625 detection. In sessions with electric stimulation, only the baseline period (i.e., before  
626 stimulation) was used for segmentation. The *PlaneCA1PC* method of sima was run on the  
627 inverted resampled movie, which resulted in detection of the hollow cell nuclei. These ROIs  
628 were then filtered based on size, and binary dilation was performed to include the  
629 cytoplasm around the nuclei. Next, the ROIs were detected in the non-inverted resampled  
630 movie and filtered based on size; those samples that did not overlap with existing ROIs  
631 were added to the set. ROIs outside the stratum pyramidale layer were excluded. The  
632 fluorescence intensity traces were then extracted for each ROI by averaging the included  
633 pixel intensities within each frame. For analyzing the run responses, only sessions with no  
634 electric stimuli were included, and signals were pulled from the motion-corrected movies.  
635 These raw traces were then processed following standard steps for obtaining  $\Delta F/F_0$  traces,  
636 with a modified approach for determining the time-dependent baseline. A 3rd-degree  
637 polynomial was fit to the trace after applying temporal smoothing, removing peaks  
638 (detected using continuous wavelet transform with `scipy.signal`), eliminating periods of  
639 running, and ignoring the beginning and end of the recording. The calculated polynomial  
640 was then used as a baseline. Z-scored traces were obtained after determining the standard  
641 deviation (SD) of each cell's baseline and excluding events exceeding 2 SDs in two  
642 iterations.

643 To analyze spreading activity, only sessions with an electric stimulus that triggered an  
644 electrographic seizure and a spreading wave were included. The segmentation was  
645 performed based on the motion-corrected baseline segments of the recordings, and the  
646 signals were pulled from non-motion-corrected movies, as image-based motion correction  
647 was not feasible during seizures.  $\Delta F/F_0$  traces were obtained using a constant baseline  
648 determined by averaging the pre-stimulus segments of the traces. To analyze changes in  
649 average fluorescence intensity, a single large ROI was manually drawn to include the cell  
650 bodies within the pyramidal layer, and  $\Delta F/F_0$  traces were obtained and processed as  
651 described above. Event-triggered averages were calculated after automatically detecting  
652 the frames with running onsets and stops using criteria that were fixed across all sessions.  
653 The average was computed in two steps; first, the events were averaged by cell, and then  
654 the cells were averaged by sensor (e.g., eCB2.0 or eCBmut). Decay time constants were  
655 computed as the parameter of a 2nd-degree polynomial fit after a log transform on the  
656 trace following the peak of the stop-triggered average trace. Rise times were determined  
657 between the frame in which the start-triggered average signal first reached 90% of the  
658 range between baseline and peak and the last frame before the signal dropped below 10%  
659 of the range. To determine the speed and direction of the spreading waves, the peak time  
660 of the wave was determined in each session by inspecting the average  $\Delta F/F_0$  trace  
661 (including all cells). Next, the relative peak location ( $\Delta t$ ) of the  $\Delta F/F_0$  trace of each cell in  
662 the trace including 200 frames (12.8 s) before and after the wave peak was determined.  
663 Finally, two linear (i.e., 1D) fits were determined using the x and y centroid coordinates of  
664 each ROI ( $\Delta t \sim x$ ,  $\Delta t \sim y$ ). The 2D speed was then computed from the slopes of the two 1D  
665 fits. The direction was determined by computing the unity vector from the starting point to  
666 the end point of the fits between 3 s before and after the wave peak. The average speed  
667 was obtained by averaging the speed of individual sessions, and the average direction was

668 obtained from the sum of the unity vectors of individual sessions. Data were plotted using  
669 Python and OriginPro 2020.

670

### 671 **Statistical analysis**

672 All summary data are presented as the mean  $\pm$  s.e.m. Group data were analyzed using the  
673 Student's *t* test or one-way ANOVA. \**p* < 0.05, \*\**p* < 0.01, \*\*\**p* < 0.001, and n.s., not  
674 significant (*p* > 0.05).

675

### 676 **Data and software availability**

677 Plasmids for expressing eCB2.0 and eCBmut used in this study were deposited at  
678 Addgene ([https://www.addgene.org/Yulong\\_Li/](https://www.addgene.org/Yulong_Li/)).

679

680

### 681 **ACKNOWLEDGMENTS**

682 This work was supported by the Beijing Municipal Science & Technology Commission  
683 (Z181100001318002, Z181100001518004), the National Natural Science Foundation of  
684 China (31925017), the NIH BRAIN Initiative (NS103558), the Shenzhen-Hong Kong  
685 Institute of Brain Science (NYKFKT2019013), and the Peking-Tsinghua Center for Life  
686 Sciences and the State Key Laboratory of Membrane Biology at Peking University School  
687 of Life Sciences to Y.L.; the NIAAA (ZIA AA000416) to D.M.L; the NIH BRAIN Initiative  
688 (NS103558) to J.D.; the NIH (R01MH101214 and R01NS104944) to B.L.; the American  
689 Epilepsy Society (postdoctoral fellowship) and the NIH (K99NS117795) to B.D.; the  
690 Canadian Institutes for Health Research (postdoctoral fellowship) to J.S.F.; and the NIH to  
691 I.S. (NS99457). We thank Li lab members and alumni for helpful discussions. We thank Yi  
692 Rao for use of the 2-photon microscope, Xiaoguang Lei at PKU-CLS and the National  
693 Center for Protein Sciences at Peking University for support and assistance with the Opera  
694 Phenix high-content screening system.

695

### 696 **AUTHOR CONTRIBUTIONS**

697 Y.L. conceived the project. A.D., K.H., H.L.P., R.C., and J.D. performed the experiments  
698 related to developing, optimizing, and characterizing the sensors in cultured HEK293T cells  
699 and neurons. L.J.D. performed the surgery and photometry recording experiments related  
700 to the validation of the sensor in DLS brain slices under the supervision of D.M.L. A.D.  
701 performed the surgery and 2-photon imaging in the hippocampal brain slices. E.A.  
702 performed the surgery and 2-photon imaging in the striatal brain slices under the  
703 supervision of J.D. W. G. performed fiber photometry recordings in freely moving mice  
704 during foot shock under the supervision of B.L. B.D. and J.S.F. performed the *in vivo* 2-  
705 photon imaging in the hippocampus in mice during running and seizure under the  
706 supervision of I.S. All authors contributed to the data interpretation and analysis. A.D. and  
707 Y.L. wrote the manuscript with input from other authors.

708

### 709 **COMPETING FINANCIAL INTERESTS**

710 Y. L. has filed patent applications, the value of which might be affected by this publication.  
711

712 **REFERENCES**

- 713 1 Zuardi, A. W. History of cannabis as a medicine: a review. *Braz J Psychiatry* **28**, 153-157,  
714 doi:10.1590/s1516-44462006000200015 (2006).
- 715 2 Piomelli, D. The molecular logic of endocannabinoid signalling. *Nat Rev Neurosci* **4**, 873-  
716 884, doi:10.1038/nrn1247 (2003).
- 717 3 Wilson, R. I. & Nicoll, R. A. Endocannabinoid signaling in the brain. *Science* **296**, 678-682,  
718 doi:10.1126/science.1063545 (2002).
- 719 4 Kano, M., Ohno-Shosaku, T., Hashimotodani, Y., Uchigashima, M. & Watanabe, M.  
720 Endocannabinoid-mediated control of synaptic transmission. *Physiological reviews* **89**, 309-380,  
721 doi:10.1152/physrev.00019.2008 (2009).
- 722 5 Hebert-Chatelain, E. et al. A cannabinoid link between mitochondria and memory. *Nature*  
723 **539**, 555-559, doi:10.1038/nature20127 (2016).
- 724 6 Benard, G. et al. Mitochondrial CB(1) receptors regulate neuronal energy metabolism. *Nat*  
725 *Neurosci* **15**, 558-564, doi:10.1038/nn.3053 (2012).
- 726 7 Jimenez-Blasco, D. et al. Glucose metabolism links astroglial mitochondria to cannabinoid  
727 effects. *Nature* **583**, 603-608, doi:10.1038/s41586-020-2470-y (2020).
- 728 8 Stella, N. Cannabinoid signaling in glial cells. *Glia* **48**, 267-277, doi:10.1002/glia.20084  
729 (2004).
- 730 9 Navarrete, M., Diez, A. & Araque, A. Astrocytes in endocannabinoid signalling. *Philos*  
731 *Trans R Soc Lond B Biol Sci* **369**, 20130599, doi:10.1098/rstb.2013.0599 (2014).
- 732 10 Chevaleyre, V., Takahashi, K. A. & Castillo, P. E. Endocannabinoid-mediated synaptic  
733 plasticity in the CNS. *Annu Rev Neurosci* **29**, 37-76,  
734 doi:10.1146/annurev.neuro.29.051605.112834 (2006).
- 735 11 Oddi, S., Scipioni, L. & Maccarrone, M. Endocannabinoid system and adult neurogenesis:  
736 a focused review. *Curr Opin Pharmacol* **50**, 25-32, doi:10.1016/j.coph.2019.11.002 (2020).
- 737 12 Moreira, F. A. & Lutz, B. The endocannabinoid system: emotion, learning and addiction.  
738 *Addict Biol* **13**, 196-212, doi:10.1111/j.1369-1600.2008.00104.x (2008).
- 739 13 Guindon, J. & Hohmann, A. G. The endocannabinoid system and pain. *CNS Neurol Disord*  
740 *Drug Targets* **8**, 403-421 (2009).
- 741 14 Kesner, A. J. & Lovinger, D. M. Cannabinoids, Endocannabinoids and Sleep. *Frontiers in*  
742 *molecular neuroscience* **13**, 125, doi:10.3389/fnmol.2020.00125 (2020).
- 743 15 Silvestri, C. & Di Marzo, V. The endocannabinoid system in energy homeostasis and the  
744 etiopathology of metabolic disorders. *Cell Metab* **17**, 475-490, doi:10.1016/j.cmet.2013.03.001  
745 (2013).
- 746 16 Katona, I. & Freund, T. F. Endocannabinoid signaling as a synaptic circuit breaker in  
747 neurological disease. *Nat Med* **14**, 923-930, doi:10.1038/nm.f.1869 (2008).
- 748 17 Fernandez-Espejo, E., Viveros, M. P., Nunez, L., Ellenbroek, B. A. & Rodriguez de  
749 Fonseca, F. Role of cannabis and endocannabinoids in the genesis of schizophrenia.  
750 *Psychopharmacology (Berl)* **206**, 531-549, doi:10.1007/s00213-009-1612-6 (2009).
- 751 18 Fraguas-Sanchez, A. I., Martin-Sabroso, C. & Torres-Suarez, A. I. Insights into the effects  
752 of the endocannabinoid system in cancer: a review. *Br J Pharmacol* **175**, 2566-2580,  
753 doi:10.1111/bph.14331 (2018).
- 754 19 Patel, S., Hill, M. N., Cheer, J. F., Wotjak, C. T. & Holmes, A. The endocannabinoid system  
755 as a target for novel anxiolytic drugs. *Neurosci Biobehav Rev* **76**, 56-66,

- 756 doi:10.1016/j.neubiorev.2016.12.033 (2017).
- 757 20 Ligresti, A., Petrosino, S. & Di Marzo, V. From endocannabinoid profiling to  
758 'endocannabinoid therapeutics'. *Curr Opin Chem Biol* **13**, 321-331,  
759 doi:10.1016/j.cbpa.2009.04.615 (2009).
- 760 21 Sabatini, B. L. & Regehr, W. G. Timing of synaptic transmission. *Annu Rev Physiol* **61**,  
761 521-542, doi:10.1146/annurev.physiol.61.1.521 (1999).
- 762 22 Zoerner, A. A. et al. Quantification of endocannabinoids in biological systems by  
763 chromatography and mass spectrometry: a comprehensive review from an analytical and  
764 biological perspective. *Biochim Biophys Acta* **1811**, 706-723, doi:10.1016/j.bbapap.2011.08.004  
765 (2011).
- 766 23 Marchioni, C. et al. Recent advances in LC-MS/MS methods to determine  
767 endocannabinoids in biological samples: Application in neurodegenerative diseases. *Anal Chim  
768 Acta* **1044**, 12-28, doi:10.1016/j.aca.2018.06.016 (2018).
- 769 24 Wilson, R. I. & Nicoll, R. A. Endogenous cannabinoids mediate retrograde signalling at  
770 hippocampal synapses. *Nature* **410**, 588-592, doi:10.1038/35069076 (2001).
- 771 25 Kreitzer, A. C. & Regehr, W. G. Retrograde inhibition of presynaptic calcium influx by  
772 endogenous cannabinoids at excitatory synapses onto Purkinje cells. *Neuron* **29**, 717-727  
773 (2001).
- 774 26 Maejima, T., Hashimoto, K., Yoshida, T., Aiba, A. & Kano, M. Presynaptic inhibition caused  
775 by retrograde signal from metabotropic glutamate to cannabinoid receptors. *Neuron* **31**, 463-  
776 475 (2001).
- 777 27 Ohno-Shosaku, T., Maejima, T. & Kano, M. Endogenous cannabinoids mediate retrograde  
778 signals from depolarized postsynaptic neurons to presynaptic terminals. *Neuron* **29**, 729-738  
779 (2001).
- 780 28 Wiskerke, J. et al. Characterization of the effects of reuptake and hydrolysis inhibition on  
781 interstitial endocannabinoid levels in the brain: an in vivo microdialysis study. *ACS Chem  
782 Neurosci* **3**, 407-417, doi:10.1021/cn300036b (2012).
- 783 29 Walker, J. M., Huang, S. M., Strangman, N. M., Tsou, K. & Sanudo-Pena, M. C. Pain  
784 modulation by release of the endogenous cannabinoid anandamide. *Proc Natl Acad Sci U S A*  
785 **96**, 12198-12203, doi:10.1073/pnas.96.21.12198 (1999).
- 786 30 Sun, F. et al. A Genetically Encoded Fluorescent Sensor Enables Rapid and Specific  
787 Detection of Dopamine in Flies, Fish, and Mice. *Cell* **174**, 481-496 e419,  
788 doi:10.1016/j.cell.2018.06.042 (2018).
- 789 31 Patriarchi, T. et al. Ultrafast neuronal imaging of dopamine dynamics with designed  
790 genetically encoded sensors. *Science* **360**, doi:10.1126/science.aat4422 (2018).
- 791 32 Jing, M. et al. A genetically encoded fluorescent acetylcholine indicator for in vitro and in  
792 vivo studies. *Nat Biotechnol* **36**, 726-737, doi:10.1038/nbt.4184 (2018).
- 793 33 Feng, J. et al. A Genetically Encoded Fluorescent Sensor for Rapid and Specific In Vivo  
794 Detection of Norepinephrine. *Neuron* **102**, 745-761 e748, doi:10.1016/j.neuron.2019.02.037  
795 (2019).
- 796 34 Peng, W. et al. Regulation of sleep homeostasis mediator adenosine by basal forebrain  
797 glutamatergic neurons. *Science* **369**, doi:10.1126/science.abb0556 (2020).
- 798 35 Patriarchi, T. et al. An expanded palette of dopamine sensors for multiplex imaging in vivo.  
799 *Nat Methods*, doi:10.1038/s41592-020-0936-3 (2020).

- 800 36 Jing, M. *et al.* An optimized acetylcholine sensor for monitoring *in vivo* cholinergic activity.  
801 *Nature Methods*, doi:10.1038/s41592-020-0953-2 (2020).
- 802 37 Sun, F. *et al.* New and improved GRAB fluorescent sensors for monitoring dopaminergic  
803 activity *<em>in vivo</em>*. 2020.2003.2028.013722, doi:10.1101/2020.03.28.013722 %J  
804 bioRxiv (2020).
- 805 38 Wan, J. *et al.* A genetically encoded GRAB sensor for measuring serotonin dynamics  
806 *<em>in vivo</em>*. 2020.2002.2024.962282, doi:10.1101/2020.02.24.962282 %J bioRxiv  
807 (2020).
- 808 39 Howlett, A. C. *et al.* International Union of Pharmacology. XXVII. Classification of  
809 cannabinoid receptors. *Pharmacol Rev* **54**, 161-202, doi:10.1124/pr.54.2.161 (2002).
- 810 40 Hua, T. *et al.* Crystal structures of agonist-bound human cannabinoid receptor CB1. *Nature*  
811 **547**, 468-471, doi:10.1038/nature23272 (2017).
- 812 41 Hua, T. *et al.* Crystal Structure of the Human Cannabinoid Receptor CB1. *Cell* **167**, 750-  
813 762 e714, doi:10.1016/j.cell.2016.10.004 (2016).
- 814 42 Krishna Kumar, K. *et al.* Structure of a Signaling Cannabinoid Receptor 1-G Protein  
815 Complex. *Cell* **176**, 448-458 e412, doi:10.1016/j.cell.2018.11.040 (2019).
- 816 43 Li, X. *et al.* Crystal Structure of the Human Cannabinoid Receptor CB2. *Cell* **176**, 459-467  
817 e413, doi:10.1016/j.cell.2018.12.011 (2019).
- 818 44 Shao, Z. *et al.* Structure of an allosteric modulator bound to the CB1 cannabinoid receptor.  
819 *Nat Chem Biol* **15**, 1199-1205, doi:10.1038/s41589-019-0387-2 (2019).
- 820 45 Shao, Z. *et al.* High-resolution crystal structure of the human CB1 cannabinoid receptor.  
821 *Nature*, doi:10.1038/nature20613 (2016).
- 822 46 Masuho, I. *et al.* Distinct profiles of functional discrimination among G proteins determine  
823 the actions of G protein-coupled receptors. *Sci Signal* **8**, ra123, doi:10.1126/scisignal.aab4068  
824 (2015).
- 825 47 Hollins, B., Kuravi, S., Digby, G. J. & Lambert, N. A. The c-terminus of GRK3 indicates  
826 rapid dissociation of G protein heterotrimers. *Cell Signal* **21**, 1015-1021,  
827 doi:10.1016/j.cellsig.2009.02.017 (2009).
- 828 48 Kroese, W. K. *et al.* PRESTO-Tango as an open-source resource for interrogation of the  
829 druggable human GPCRome. *Nat Struct Mol Biol* **22**, 362-369, doi:10.1038/nsmb.3014 (2015).
- 830 49 Kim, S. H., Won, S. J., Mao, X. O., Jin, K. & Greenberg, D. A. Molecular mechanisms of  
831 cannabinoid protection from neuronal excitotoxicity. *Mol Pharmacol* **69**, 691-696,  
832 doi:10.1124/mol.105.016428 (2006).
- 833 50 Wu, J. *et al.* Genetically Encoded Glutamate Indicators with Altered Color and Topology.  
834 *ACS Chem Biol* **13**, 1832-1837, doi:10.1021/acschembio.7b01085 (2018).
- 835 51 Alger, B. E. Retrograde signaling in the regulation of synaptic transmission: focus on  
836 endocannabinoids. *Prog Neurobiol* **68**, 247-286, doi:10.1016/s0301-0082(02)00080-1 (2002).
- 837 52 Ogasawara, D. *et al.* Rapid and profound rewiring of brain lipid signaling networks by acute  
838 diacylglycerol lipase inhibition. *Proc Natl Acad Sci U S A* **113**, 26-33,  
839 doi:10.1073/pnas.1522364112 (2016).
- 840 53 Long, J. Z. *et al.* Selective blockade of 2-arachidonoylglycerol hydrolysis produces  
841 cannabinoid behavioral effects. *Nat Chem Biol* **5**, 37-44, doi:10.1038/nchembio.129 (2009).
- 842 54 Mor, M. *et al.* Cyclohexylcarbamic acid 3'- or 4'-substituted biphenyl-3-yl esters as fatty  
843 acid amide hydrolase inhibitors: synthesis, quantitative structure-activity relationships, and

- 844 molecular modeling studies. *J Med Chem* **47**, 4998-5008, doi:10.1021/jm031140x (2004).
- 845 55 Brenowitz, S. D. & Regehr, W. G. Associative short-term synaptic plasticity mediated by
- 846 endocannabinoids. *Neuron* **45**, 419-431, doi:10.1016/j.neuron.2004.12.045 (2005).
- 847 56 Soler-Llavina, G. J. & Sabatini, B. L. Synapse-specific plasticity and compartmentalized
- 848 signaling in cerebellar stellate cells. *Nat Neurosci* **9**, 798-806, doi:10.1038/nn1698 (2006).
- 849 57 Lerner, T. N. & Kreitzer, A. C. RGS4 is required for dopaminergic control of striatal LTD and
- 850 susceptibility to parkinsonian motor deficits. *Neuron* **73**, 347-359,
- 851 doi:10.1016/j.neuron.2011.11.015 (2012).
- 852 58 Gerdeman, G. L., Ronesi, J. & Lovinger, D. M. Postsynaptic endocannabinoid release is
- 853 critical to long-term depression in the striatum. *Nat Neurosci* **5**, 446-451, doi:10.1038/nn832
- 854 (2002).
- 855 59 Kreitzer, A. C. & Malenka, R. C. Endocannabinoid-mediated rescue of striatal LTD and
- 856 motor deficits in Parkinson's disease models. *Nature* **445**, 643-647, doi:10.1038/nature05506
- 857 (2007).
- 858 60 Yasuda, H., Huang, Y. & Tsumoto, T. Regulation of excitability and plasticity by
- 859 endocannabinoids and PKA in developing hippocampus. *Proc Natl Acad Sci U S A* **105**, 3106-
- 860 3111, doi:10.1073/pnas.0708349105 (2008).
- 861 61 Edwards, D. A., Zhang, L. & Alger, B. E. Metaplastic control of the endocannabinoid system
- 862 at inhibitory synapses in hippocampus. *Proc Natl Acad Sci U S A* **105**, 8142-8147,
- 863 doi:10.1073/pnas.0803558105 (2008).
- 864 62 Li, B. Central amygdala cells for learning and expressing aversive emotional memories.
- 865 *Curr Opin Behav Sci* **26**, 40-45, doi:10.1016/j.cobeha.2018.09.012 (2019).
- 866 63 Katona, I. et al. Distribution of CB1 cannabinoid receptors in the amygdala and their role
- 867 in the control of GABAergic transmission. *J Neurosci* **21**, 9506-9518 (2001).
- 868 64 Morena, M., Patel, S., Bains, J. S. & Hill, M. N. Neurobiological Interactions Between
- 869 Stress and the Endocannabinoid System. *Neuropsychopharmacology* **41**, 80-102,
- 870 doi:10.1038/npp.2015.166 (2016).
- 871 65 Gunduz-Cinar, O., Hill, M. N., McEwen, B. S. & Holmes, A. Amygdala FAAH and
- 872 anandamide: mediating protection and recovery from stress. *Trends Pharmacol Sci* **34**, 637-
- 873 644, doi:10.1016/j.tips.2013.08.008 (2013).
- 874 66 Dana, H. et al. Sensitive red protein calcium indicators for imaging neural activity. *eLife* **5**,
- 875 doi:10.7554/eLife.12727 (2016).
- 876 67 Soltesz, I. et al. Weeding out bad waves: towards selective cannabinoid circuit control in
- 877 epilepsy. *Nat Rev Neurosci* **16**, 264-277, doi:10.1038/nrn3937 (2015).
- 878 68 Farrell, J. S. et al. In vivo assessment of mechanisms underlying the neurovascular basis
- 879 of postictal amnesia. *Sci Rep* **10**, 14992, doi:10.1038/s41598-020-71935-6 (2020).
- 880 69 Heinbockel, T. et al. Endocannabinoid signaling dynamics probed with optical tools. *J*
- 881 *Neurosci* **25**, 9449-9459, doi:10.1523/JNEUROSCI.2078-05.2005 (2005).
- 882 70 Ju, N. et al. Spatiotemporal functional organization of excitatory synaptic inputs onto
- 883 macaque V1 neurons. *Nat Commun* **11**, 697, doi:10.1038/s41467-020-14501-y (2020).
- 884 71 Sethuramanujam, S. et al. Rapid 'multi-directed' cholinergic transmission at central
- 885 synapses. 2020.2004.2018.048330, doi:10.1101/2020.04.18.048330 %J bioRxiv (2020).
- 886 72 Kaifosh, P., Lovett-Barron, M., Turi, G. F., Reardon, T. R. & Losonczy, A. Septo-
- 887 hippocampal GABAergic signaling across multiple modalities in awake mice. *Nat Neurosci* **16**,

- 888 1182-1184, doi:10.1038/nn.3482 (2013).
- 889 73 Lovett-Barron, M. *et al.* Dendritic inhibition in the hippocampus supports fear learning.
- 890 *Science* **343**, 857-863, doi:10.1126/science.1247485 (2014).
- 891 74 Farrell, J. S. *et al.* Postictal behavioural impairments are due to a severe prolonged
- 892 hypoperfusion/hypoxia event that is COX-2 dependent. *eLife* **5**, doi:10.7554/eLife.19352 (2016).
- 893 75 Kaifosh, P., Zaremba, J. D., Danielson, N. B. & Losonczy, A. SIMA: Python software for
- 894 analysis of dynamic fluorescence imaging data. *Front Neuroinform* **8**, 80,
- 895 doi:10.3389/fninf.2014.00080 (2014).
- 896

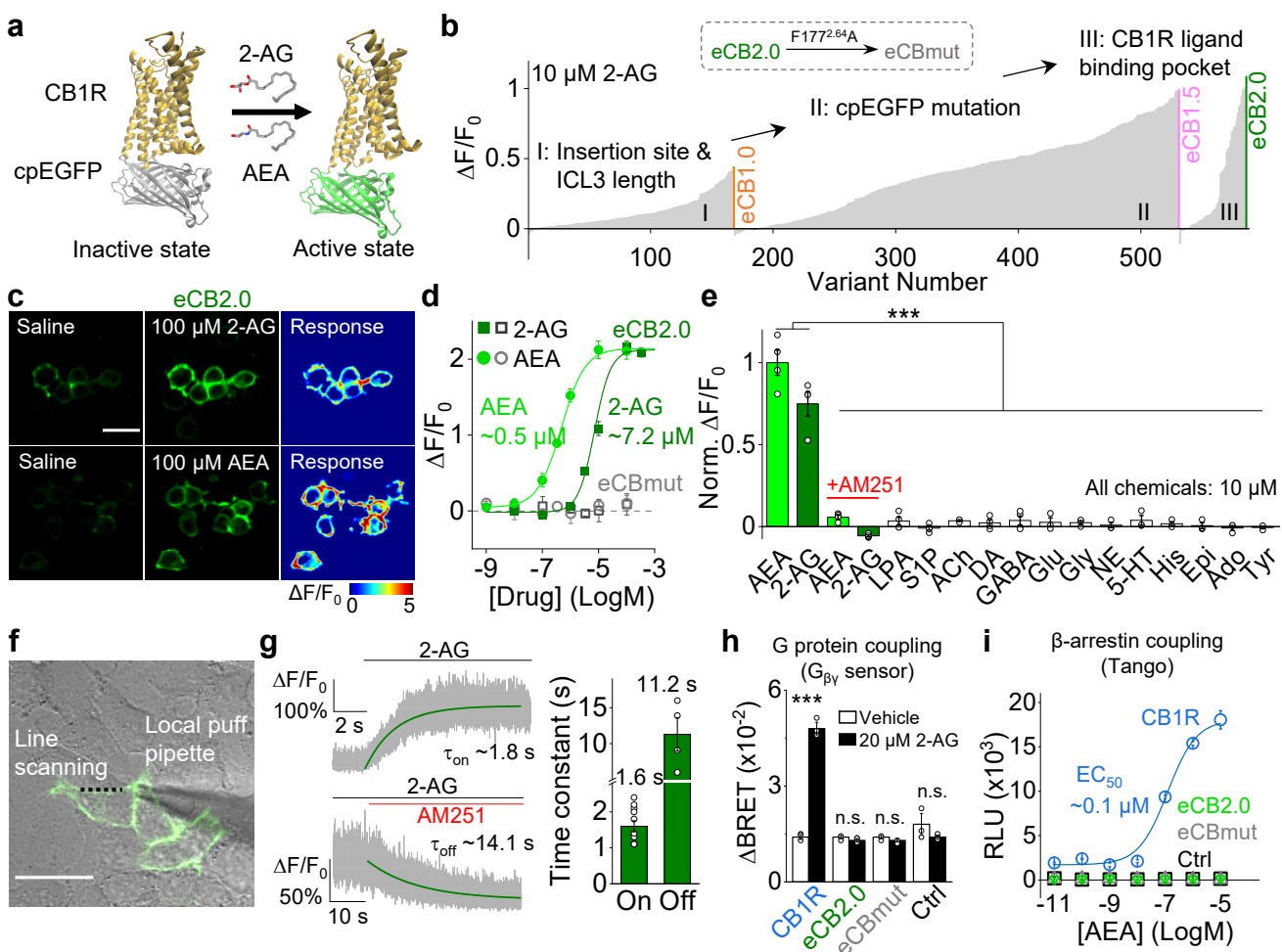


**Fig. 1 | Development, optimization, and characterization of GRAB<sub>eCB</sub> sensors in HEK293T cells**

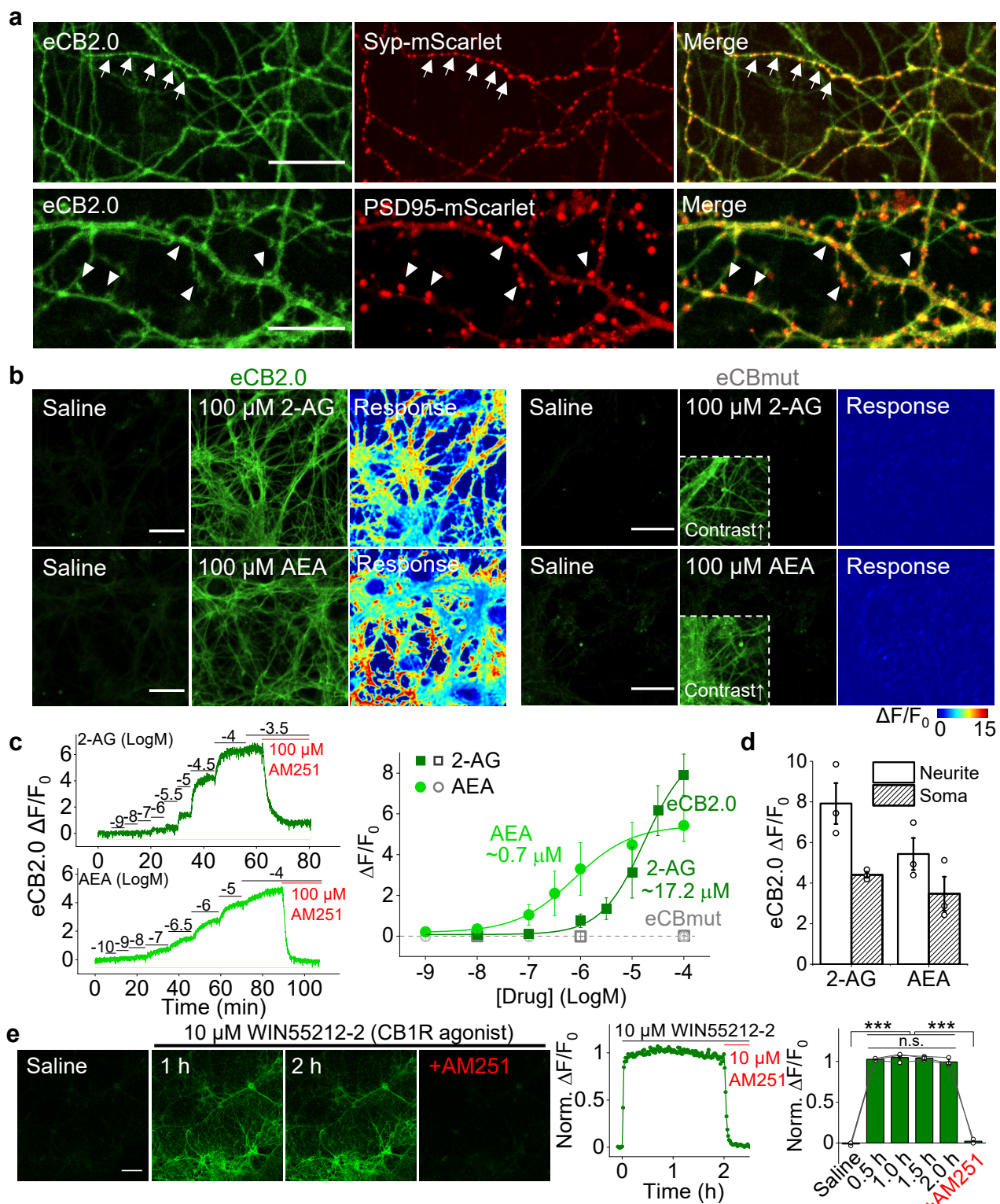


**Fig. 2 | Characterization of GRAB<sub>eCB</sub> sensors in primary cultured neurons**

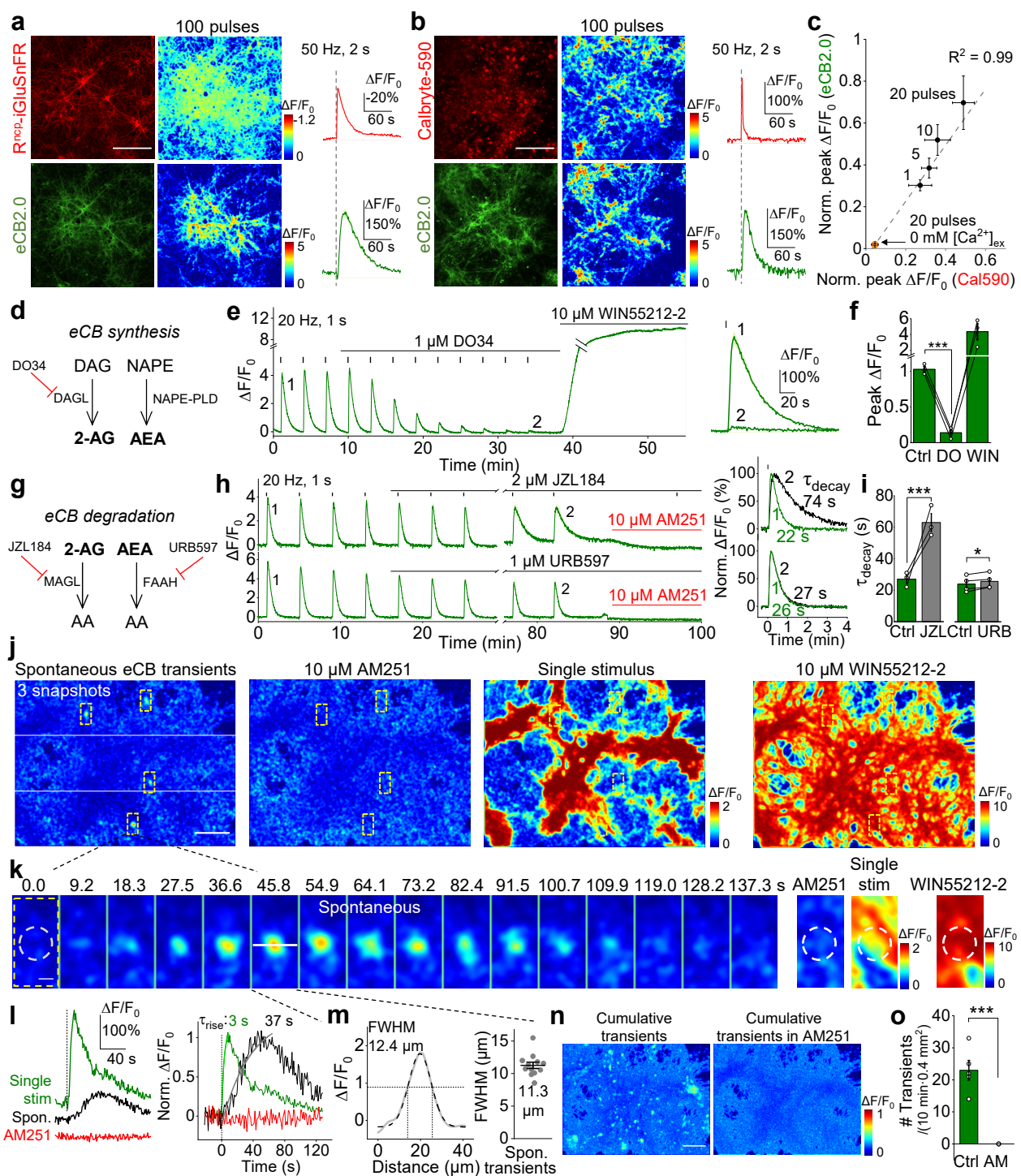


**Fig. 3 | Release of endogenous eCB measured in primary cultured neurons**

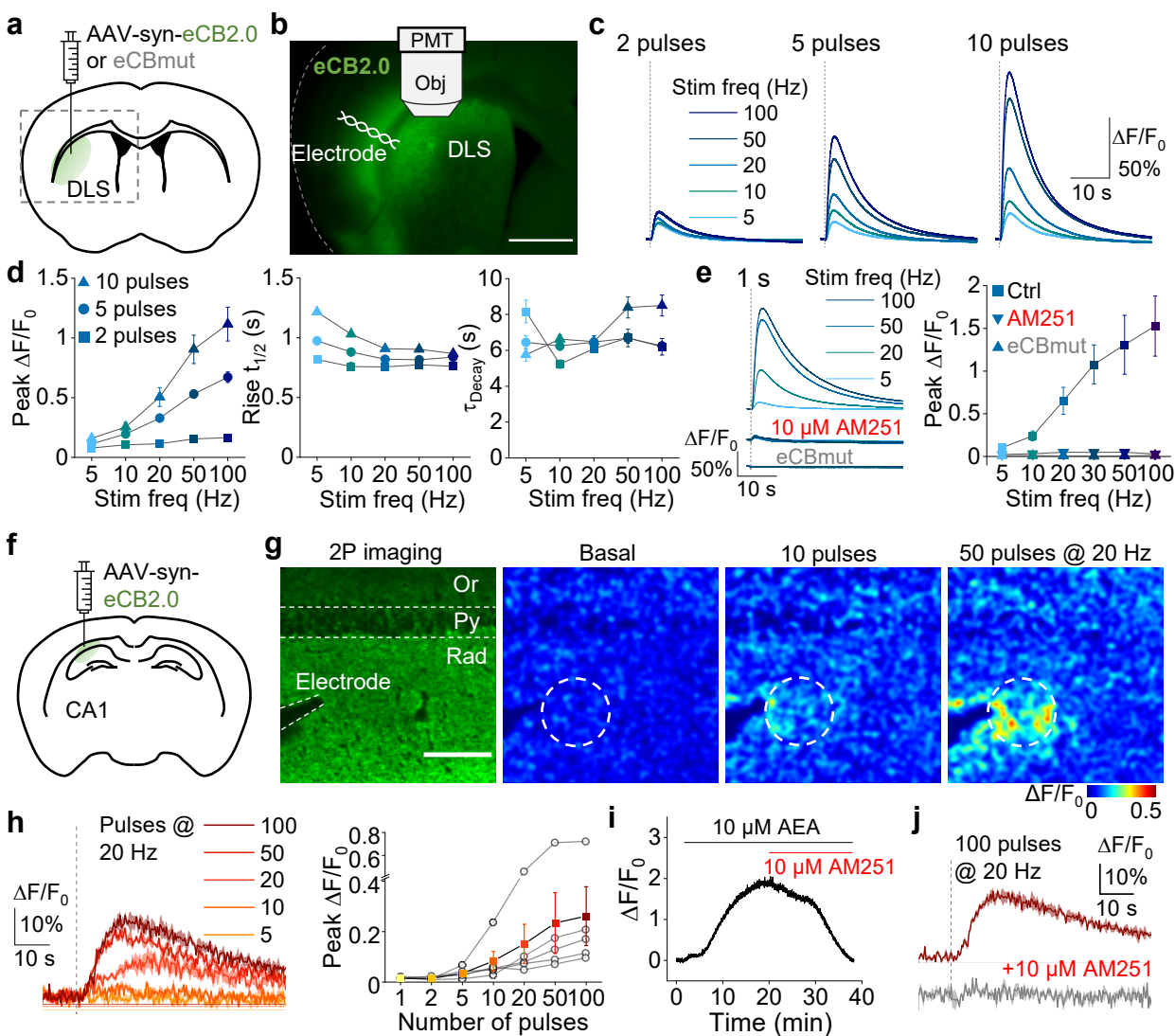


**Fig. 4 | Using the GRAB<sub>eCB</sub> sensor to detect eCB release in acute brain slices**

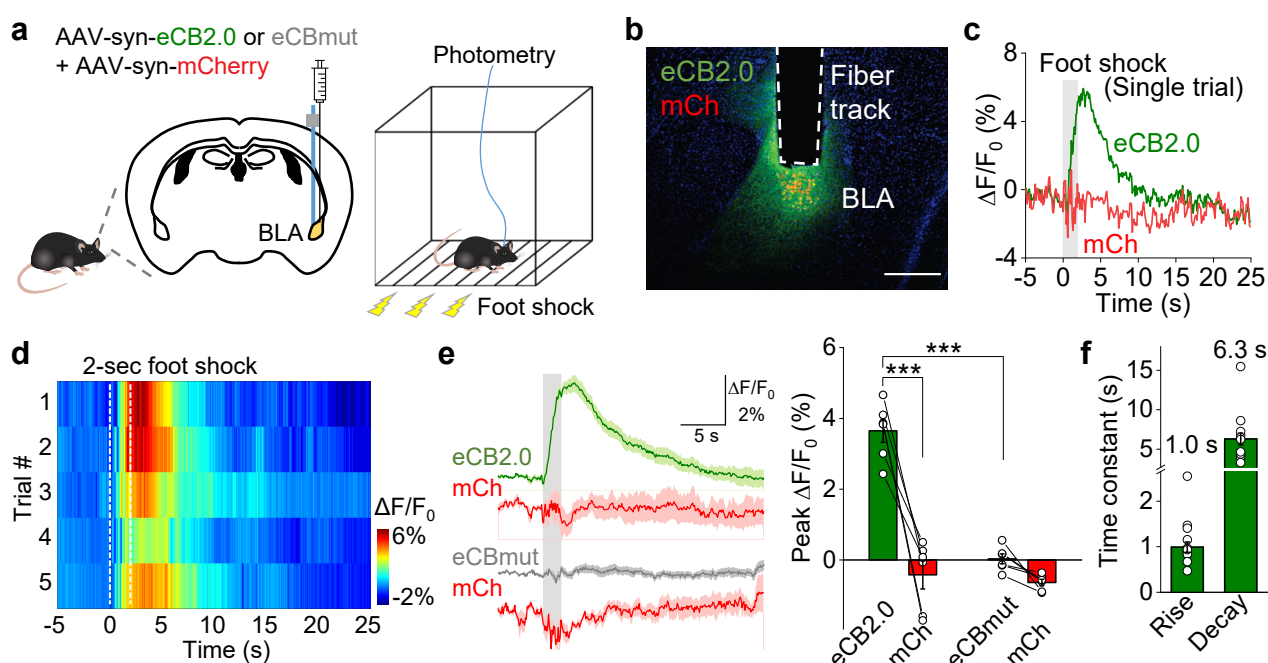


**Fig. 5 | Measuring *in vivo* eCB signals in the mouse basolateral amygdala in response to foot shock**

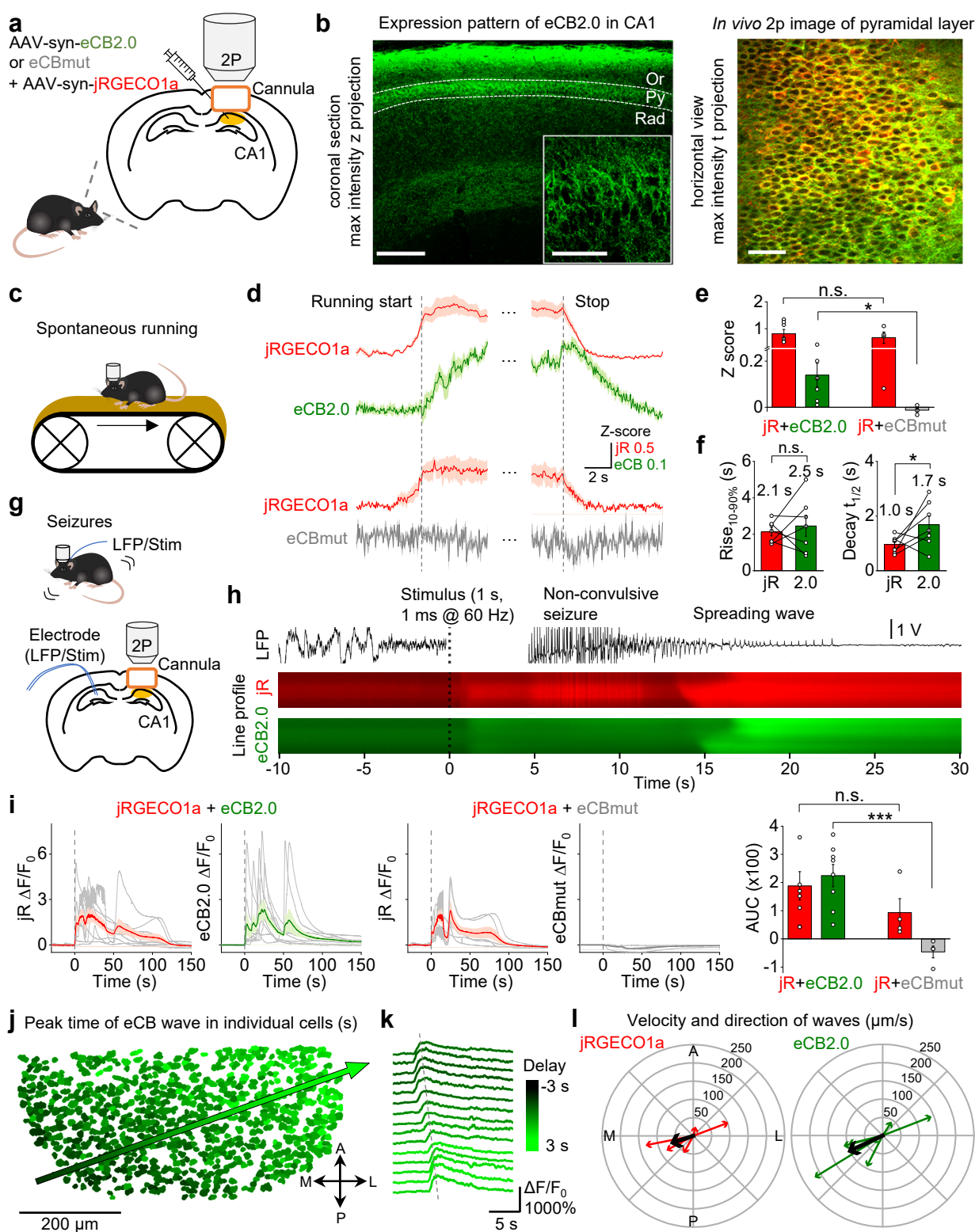
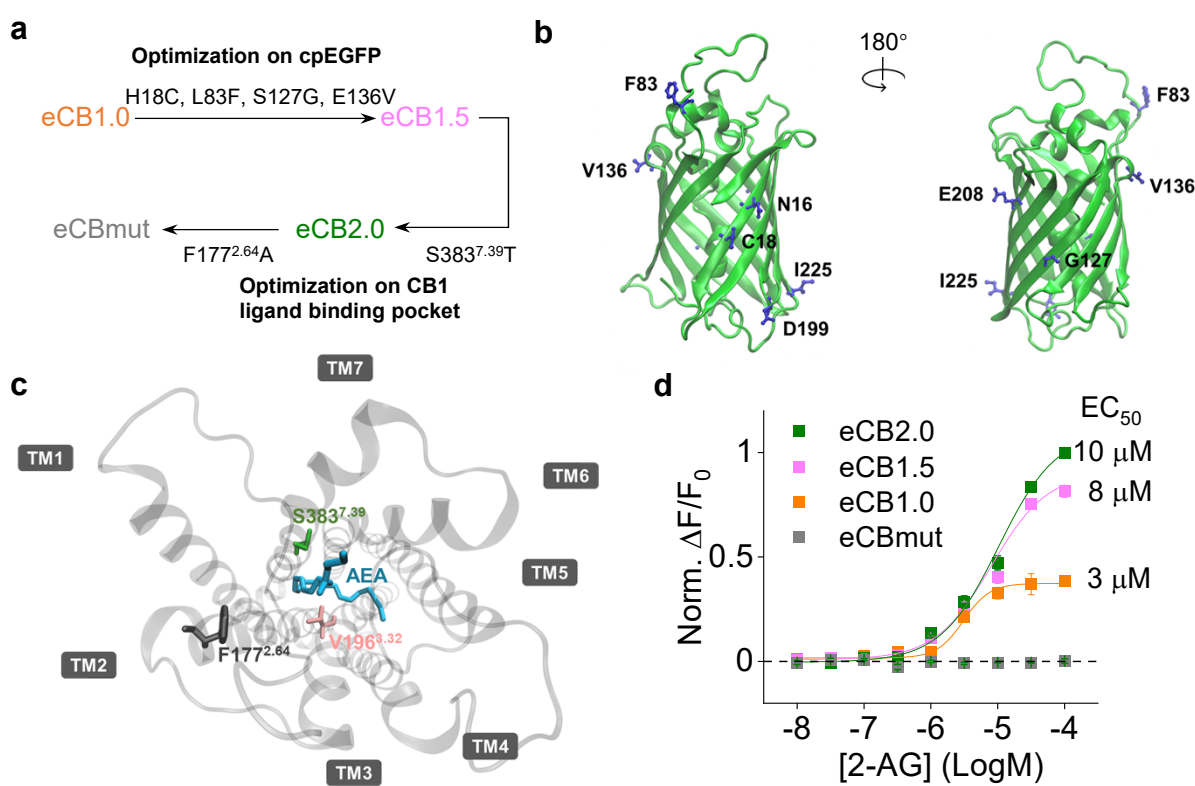
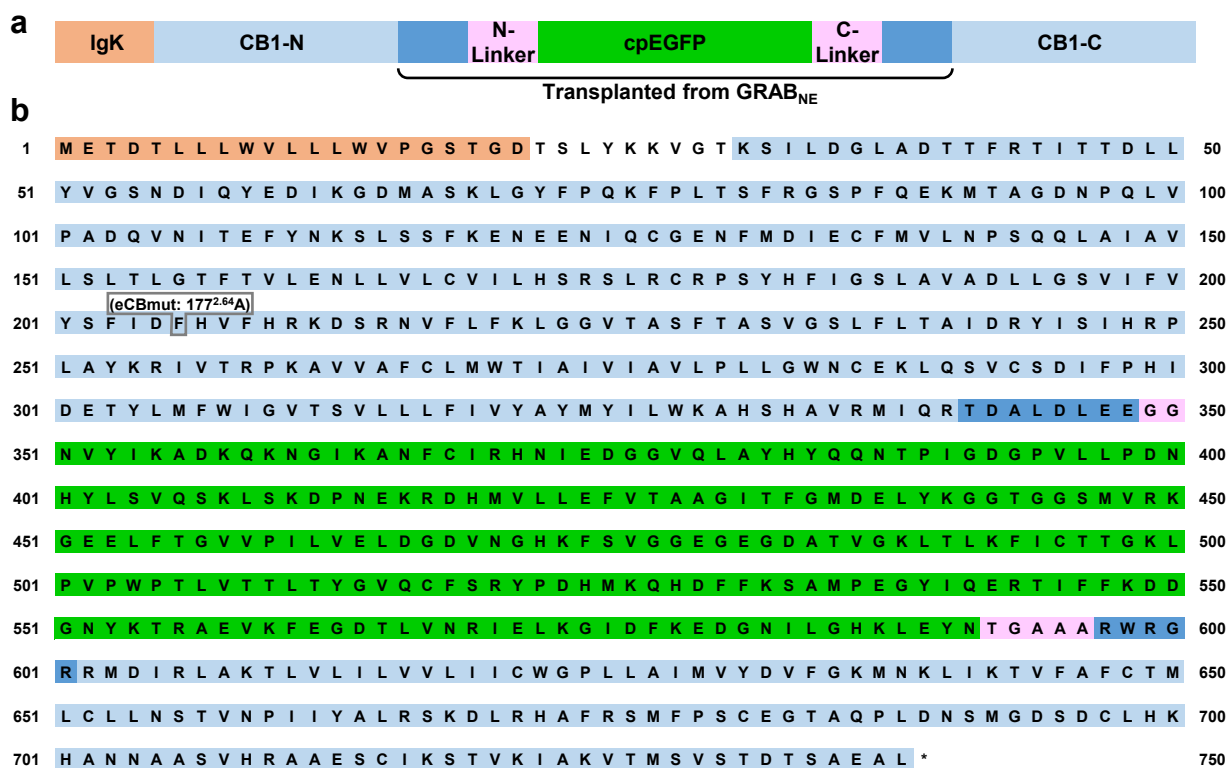


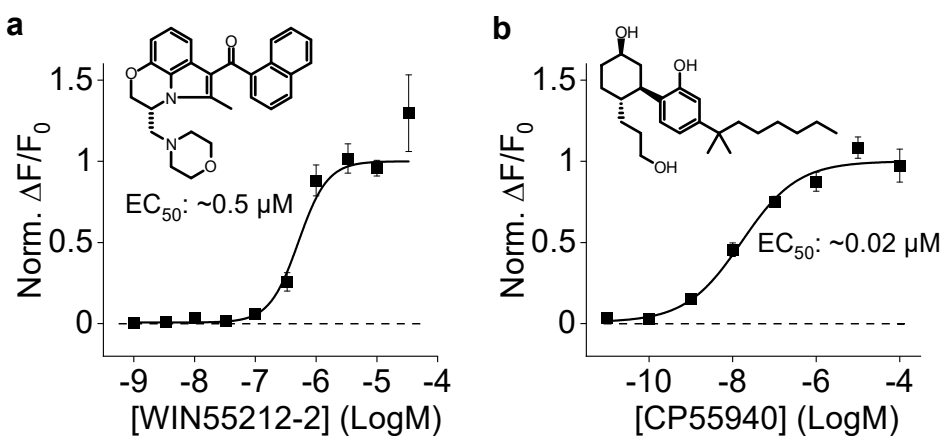
**Fig. 6 | Measuring *in vivo* eCB dynamics in the mouse hippocampus during running and seizure activity**



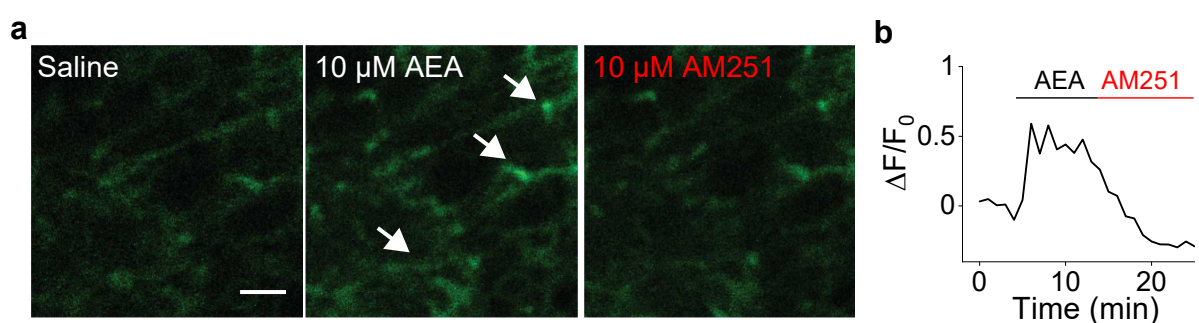
**Extended Data Fig. 1 | Strategy for optimizing and screening the GRABeCB sensor prototypes**



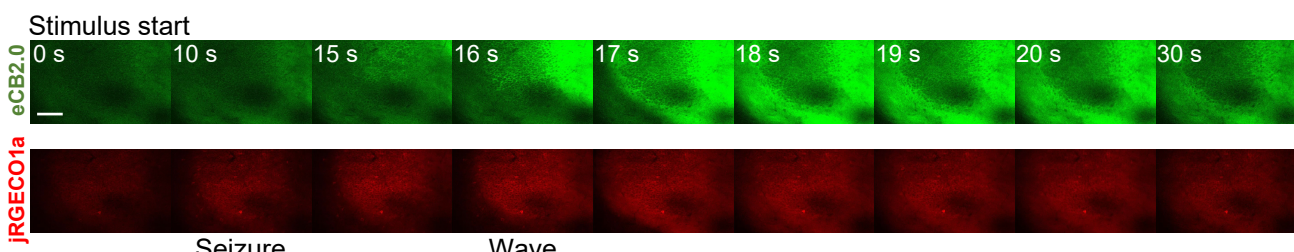
## Extended Data Fig. 2 | Full amino acid sequences of the eCB2.0 and eCBmut sensors



**Extended Data Fig. 3 | The eCB2.0 responses to synthetic CB1R agonists**



**Extended Data Fig. 4 | 2P imaging of eCB2.0 in acute mouse striatal slices**



**Extended Data Fig. 5 | eCB and  $\text{Ca}^{2+}$  waves in mouse hippocampal CA1 region during seizure activity**

897 **FIGURE LEGENDS**

898

899 **Fig. 1 | Development, optimization, and characterization of GRAB<sub>eCB</sub> sensors in**  
900 **HEK293T cells**

901 **a**, Schematic diagram depicting the design and principle of the GRAB<sub>eCB</sub> sensor, consisting  
902 of the CB1 receptor and circular-permuted GFP. Ligand binding activates the sensor,  
903 inducing a change in fluorescence.

904 **b**, Screening and optimization steps of GRAB<sub>eCB</sub> sensors and the normalized fluorescence  
905 response to 10 μM 2-AG. eCBmut was generated by introducing the F177<sup>2,64</sup>A mutation in  
906 eCB2.0.

907 **c**, Expression and fluorescence change in response to 100 μM 2-AG and AEA in HEK293T  
908 cells expressing eCB2.0. Scale bar, 30 μm.

909 **d**, Dose-response curves measured in HEK293T cells expressing eCB2.0 or eCBmut, with  
910 the corresponding EC<sub>50</sub> values for 2-AG and AEA shown; n = 3 wells each.

911 **e**, Normalized fluorescence change in response to the indicated compounds (each at 10  
912 μM) measured in cells expressing eCB2.0; n = 3–4 well each. Where indicated, the CB1R  
913 inverse agonist AM251 was also added. LPA, lysophosphatidic acid; S1P, sphingosine-1-  
914 phosphate; ACh, acetylcholine; DA, dopamine; GABA, gamma-aminobutyric acid; Glu,  
915 glutamate; Gly, glycine; NE, norepinephrine; 5-HT, 5-hydroxytryptamine; His, histamine;  
916 Epi, epinephrine; Ado, adenosine; Tyr, tyramine.

917 **f**, Illustration of the localized puffing system using a glass pipette containing 100 μM 2-AG  
918 and/or AM251 positioned above an eCB2.0-expressing cell. The dotted black line indicates  
919 the region of interest for line scanning. Scale bar, 30 μm.

920 **g**, Change in eCB2.0 fluorescence was measured in an eCB2.0-expressing cell using line  
921 scanning; where indicated, 2-AG and AM251 were puffed on the cell. The graph at the right  
922 summarizes the on and off time constants measured upon application of 2-AG and upon  
923 application of AM251, respectively; n = 11 ( $\tau_{on}$ ) and 4 ( $\tau_{off}$ ) cells.

924 **h**, G protein coupling was measured using a BRET G<sub>βγ</sub> sensor in cells expressing CB1R,  
925 eCB2.0, or eCBmut.

926 **i**, β-arrestin coupling was measured using the Tango assay in cells expressing CB1R,  
927 eCB2.0, or eCBmut.

928 Student's t tests were performed in **e** and **h**: \*\*\*p < 0.001; n.s., not significant.

929

930 **Fig. 2 | Characterization of GRAB<sub>eCB</sub> sensors in primary cultured neurons**

931 **a**, Fluorescence microscopy images of primary cultured rat cortical neurons expressing  
932 eCB2.0 (green) and either synaptophysin-mScarlet (top row; red) or PSD95-mScarlet  
933 (bottom row; red). In the top row, arrows indicate axons; in the bottom row, arrowheads  
934 indicate dendrites and dendritic spines. Scale bars, 30  $\mu$ m (top row) and 15  $\mu$ m (bottom  
935 row).

936 **b**, Fluorescence microscopy images and fluorescence response to 100  $\mu$ M 2-AG (top row)  
937 or AEA (bottom row) in neurons expressing eCB2.0 (left) or eCBmut (right). The insets in  
938 the eCBmut images are contrast-enhanced to show expression of the sensor. Scale bars,  
939 30  $\mu$ m.

940 **c**, (Left) example traces of  $\Delta F/F_0$  measured in an eCB2.0-expressing neuron; the indicated  
941 concentrations of 2-AG and AEA, followed by 100  $\mu$ M AM251, were applied. (Right) dose-  
942 response curves measured in neurons expressing eCB2.0 or eCBmut, with the  
943 corresponding EC<sub>50</sub> values shown; n = 3 cultures each.

944 **d**, Summary of the change in eCB2.0 fluorescence in response to 100  $\mu$ M 2-AG or AEA  
945 measured in the neurites and soma; n = 3 cultures each.

946 **e**, Example images (left), trace (middle), and quantification (right) of the change in eCB2.0  
947 fluorescence in response to a 2-hour application of WIN55212-2, followed by AM251; n =  
948 3 cultures each. Scale bar, 100  $\mu$ m.

949 Student's *t* test and one-way ANOVA were performed in **e**: \*\*\*p < 0.001; n.s., not significant.  
950

951 **Fig. 3 | Release of endogenous eCB measured in primary cultured neurons**

952 **a**, Fluorescence microscopy images and fluorescence response measured in neurons co-  
953 expressing R<sup>ncp</sup>-iGluSnFR (red) and eCB2.0 (green). Scale bar, 200  $\mu$ m.  
954 **b**, Fluorescence microscopy images and fluorescence response measured in eCB2.0-  
955 expressing cells preloaded with Calbryte-590 (red). Scale bar, 200  $\mu$ m.  
956 **c**, Relative peak change in eCB2.0 fluorescence plotted against the relative peak change  
957 in Calbryte590 fluorescence measured in response to the indicated number of electrical  
958 pulses, normalized to the response evoked by 200 pulses; n = 4 cultures each. Also shown  
959 is the response to 20 electrical pulses with no extracellular Ca<sup>2+</sup>.  
960 **d**, Diagram depicting the pathway for eCB synthesis. DAG, diacylglycerol; DAGL,  
961 diacylglycerol lipase; NAPE, N-arachidonoyl phosphatidylethanolamine; NAPE-PLD,  
962 NAPE-hydrolyzing phospholipase D.  
963 **e**, Representative traces (left) and expanded traces (right) showing the change in eCB2.0  
964 fluorescence in responses to 20 electrical pulses applied before (1) and after (2) DO34  
965 application; WIN55212-2 was applied at the end of the experiment.  
966 **f**, Summary of the peak change in eCB2.0 fluorescence in response to 20 pulses applied  
967 at baseline (Ctrl), 26 min after DO34 application, and after WIN55212-2 application; n = 3  
968 cultures each.  
969 **g**, Diagram depicting the degradation pathways for 2-AG and AEA. AA, arachidonic acid;  
970 MAGL, monoacylglycerol lipase; FAAH, fatty acid amide hydrolase.  
971 **h**, Representative traces (left) and expanded traces (right) showing the change in eCB2.0  
972 fluorescence in response to 20 electrical pulses applied before (1) and after (2) JZL184 or  
973 URB597 application; AM251 was applied at the end of the experiment.  
974 **i**, Summary of the decay time constant ( $T_{decay}$ ) measured at baseline (Ctrl) and 68 min after  
975 application of either JZL184 or URB597; n = 3 cultures each.  
976 **j**, Pseudocolor images showing spontaneous changes in eCB2.0 fluorescence transients,  
977 single pulse-evoked fluorescence change, and the change in fluorescence induced by 10  
978  $\mu$ M WIN55212-2 (note the difference in scale). Scale bar, 100  $\mu$ m.  
979 **k**, Time-lapse pseudocolor images taken from the area shown by the bottom dashed  
980 rectangle in panel **j**. Scale bar, 10  $\mu$ m.  
981 **l**, Traces from the experiment shown in panel **k**, showing the change in fluorescence  
982 measured spontaneously, induced by a single pulse, or in the presence of AM251.  
983 Normalized traces with the corresponding rise time constants are shown at the right.  
984 **m**, Spatial profile of the transient change in fluorescence shown in panel **k**. The summary  
985 data are shown at the right; n = 12 transients.  
986 **n**, Cumulative transient change in eCB2.0 fluorescence measured during 19 mins of  
987 recording in the absence (left) or presence (right) of AM251 (right). Pseudocolor images  
988 were calculated as the average temporal projection subtracted from the maximum temporal  
989 projection. Scale bar, 100  $\mu$ m.  
990 **o**, Summary of the frequency of transient changes in eCB2.0 fluorescence measured  
991 before (Ctrl) and after AM251 application; n = 5 & 3 with 10-min recording/session.  
992 Student's t tests were performed in **f**, **l** and **o**: \*p < 0.05, \*\*\*p < 0.001.  
993

994 **Fig. 4 | Using the GRAB<sub>eCB</sub> sensor to detect eCB release in acute brain slices**  
995 **a**, Schematic diagram depicting the strategy for virus injection in the dorsolateral striatum  
996 (DLS), followed by the preparation of acute brain slices used for electrical stimulation and  
997 photometry recording. The dashed box corresponds to the image shown in panel **b**.  
998 **b**, Fluorescence image of a coronal slice prepared from a mouse following injection of AAV-  
999 syn-eCB2.0 in the DLS, with a diagram showing the electrode position and photometry  
1000 recording. Scale bar, 1 mm.  
1001 **c**, Representative traces showing the change in eCB2.0 fluorescence evoked by 2, 5, or  
1002 10 electrical pulses applied at the indicated frequencies.  
1003 **d**, Peak change in eCB2.0 fluorescence (left), rise  $t_{1/2}$  (middle), and decay time constant  
1004 (right) plotted against stimulation frequency for 2, 5, and 10 pulses; n = 6 slices.  
1005 **e**, Representative traces (left) and summary of the peak change in eCB2.0 fluorescence  
1006 (right) evoked by electrical pulses at the indicated frequency in slices expressing eCB2.0  
1007 in the absence or presence of AM251 and in slices expressing eCBmut; n = 3–4 slices  
1008 each.  
1009 **f**, Schematic diagram depicting the strategy for virus injection in the hippocampal CA1  
1010 region, followed by the preparation of acute slices for electrical stimulation and 2-photon  
1011 imaging.  
1012 **g**, (Left) fluorescence image of eCB2.0 expressed in the hippocampal CA1 region, showing  
1013 the position of the stimulating electrode. (Right) pseudocolor images showing the change  
1014 in eCB2.0 fluorescence at baseline and after 10 or 50 pulses applied at 20 Hz. The dashed  
1015 circle shows the ROI for quantification. Scale bar, 100  $\mu$ m.  
1016 **h**, Representative traces and summary of the peak change in eCB2.0 fluorescence evoked  
1017 by electrical pulses applied at the indicated frequencies; n = 5 slices.  
1018 **i**, Time course of the change in eCB2.0 fluorescence; where indicated, AEA and AM251  
1019 were applied.  
1020 **j**, Representative traces of the change in eCB2.0 fluorescence evoked by electrical  
1021 stimulation in the absence and presence of AM251.  
1022

1023 **Fig. 5 | Measuring *in vivo* eCB signals in the mouse basolateral amygdala in**  
1024 **response to foot shock**

1025 **a**, Schematic diagram depicting the strategy for viral expression in the basolateral  
1026 amygdala and fiber photometry recording during foot shock.

1027 **b**, Fluorescence microscopy image showing eCB2.0 (green) and mCherry (red) expressed  
1028 in the BLA and the placement of the recording fiber; the nuclei were counterstained with  
1029 DAPI (blue). Scale bar, 300  $\mu$ m.

1030 **c**, Representative single-trial traces of the change in eCB2.0 and mCherry fluorescence;  
1031 an electrical foot shock (2-sec duration) was applied at time 0.

1032 **d**, Pseudocolor change in eCB2.0 fluorescence before and after a 2-sec foot shock. Shown  
1033 are five consecutive trials in one mouse, time-aligned to the onset of each foot shock.

1034 **e**, (Left) average traces of the change in eCB2.0 and mCherry (top) and eCBmut and  
1035 mCherry (bottom) fluorescence; the gray shaded area indicates application of an electrical  
1036 foot shock. (Right) summary of the peak change in fluorescence; n = 6 mice each.

1037 **f**, Summary of rise and decay time constants measured for the change in eCB2.0  
1038 fluorescence in response to foot shock; n = 18–21 trials in 6 animals.

1039 Student's *t* tests were performed in **e**; \*\*\**p* < 0.001.

1040

1041 **Fig. 6 | Measuring *in vivo* eCB dynamics in the mouse hippocampus during running  
1042 and seizure activity**

1043 **a**, Schematic diagram depicting the strategy for viral expression and cannula placement in  
1044 the mouse hippocampus.

1045 **b**, (Left) immunofluorescence image showing eCB2.0 expression in the hippocampal CA1  
1046 region in a coronal brain slice. Scale bars, 200  $\mu\text{m}$  and 50  $\mu\text{m}$  (inset). (Right) *In vivo* 2-  
1047 photon image of the pyramidal layer in the hippocampal CA1 region, showing eCB2.0  
1048 (green) and jRGECO1a (red) fluorescence. Scale bar, 50  $\mu\text{m}$ .

1049 **c**, Schematic cartoon illustrating the experiment in which a mouse expressing eCB2.0 and  
1050 jRGECO1a in the hippocampal CA1 is placed on a treadmill and allowed to run  
1051 spontaneously while fluorescence is measured using 2-photon microscopy.

1052 **d**, Average traces of eCB2.0/eCBmut and jRGECO1a transients recorded in the soma of  
1053 individual neurons in the pyramidal layer upon the start and stop of spontaneous running  
1054 episodes (dashed lines).

1055 **e**, Summary of the peak responses in panel **d**; n = 8 and 4 mice each for eCB2.0 and  
1056 eCBmut, respectively.

1057 **f**, Summary of the rise and decay kinetics of the jRGECO1a and eCB2.0 signals measured  
1058 at the start and end of spontaneous running; n = 7 mice.

1059 **g**, Schematic diagram depicting the electrode placement and 2-photon imaging in mice  
1060 expressing eCB2.0 and jRGECO1a in the hippocampal CA1 region; the electrode is used  
1061 to induce kindling seizure activity and to measure the local field potential (LFP).

1062 **h**, Example LFP trace (top) and medio-lateral projections (line profile) of jRGECO1a  
1063 (middle) and eCB2.0 (bottom) fluorescence during stimulus-induced non-convulsive  
1064 seizures and a subsequent spreading wave. The dashed vertical line at time 0 indicates  
1065 the stimulus onset.

1066 **i**, Individual (thin gray lines) and average (thick lines) traces of the change in jRGECO1a  
1067 and eCB2.0/eCBmut fluorescence measured during seizure activity. The dashed vertical  
1068 line at time 0 indicates the stimulus onset. The summary of the area under the curve (AUC)  
1069 is shown at the right; n = 8 and 4 for eCB2.0 and eCBmut, respectively.

1070 **j**, Spreading eCB wave measured through the hippocampal CA1 region after seizure  
1071 activity. ROIs representing individual neurons are pseudocolored based on the peak time  
1072 of their eCB2.0 signal relative to the peak time of the average signal, and the arrow shows  
1073 the direction of the wave. a, anterior; l, lateral; m, medial; p, posterior.

1074 **k**, Traces of eCB2.0 fluorescence measured in individual cells sampled systematically  
1075 along a line fitted to the spreading wave. The dashed line shows the spreading of peak  
1076 signals.

1077 **l**, Velocity and direction of the spreading jRGECO1a and eCB2.0 waves. The length of  
1078 each arrow indicates the velocity in  $\mu\text{m/s}$ . In each panel, each colored arrow indicates an  
1079 individual session, and the thick black line indicates the average. n = 7 sessions in 6 mice.  
1080 Student's *t* tests were performed in **e**, **f** and **i**: \*p < 0.05, \*\*\*p < 0.001, and n.s., not  
1081 significant.

1082

1083 **Extended Data Fig. 1 | Strategy for optimizing and screening the GRABeCB sensor  
1084 prototypes**

1085 **a**, Schematic diagram depicting the strategy used to generate the various GRAB<sub>eCB</sub>  
1086 sensors for this study, including intermediate steps.

1087 **b**, Location of the 8 residues in the cpEGFP moiety used to optimize the GRAB<sub>eCB</sub> sensor.

1088 **c**, Location of the 3 residues in the GPCR ligand-binding pocket. The receptor's seven  
1089 transmembrane domains (TM1 through TM7) and the ligand molecule (AEA) are shown.

1090 **d**, Normalized dose-response curves for the change in eCB1.0, eCB1.5, eCB2.0, and  
1091 eCBmut fluorescence in response to 2-AG measured in HEK293T cells; n = 3 wells each.

1092

1093 **Extended Data Fig. 2 | Full amino acid sequences of the eCB2.0 and eCBmut sensors**

1094 **a**, Schematic diagram depicting the structure of the GRAB<sub>eCB2.0</sub> sensor. The IgK leader  
1095 sequence and the sequence derived from GRAB<sub>NE</sub> are shown.

1096 **b**, Amino acids sequence of the eCB2.0 sensor. The phenylalanine residue at position  
1097 177<sup>2,64</sup> in the CB1 receptor was mutated to an alanine to generate the eCB mutant sensor  
1098 (indicated by the gray box). Note that the numbering used in the figure corresponds to the  
1099 start of the IgK leader sequence.

1100

1101 **Extended Data Fig. 3 | The eCB2.0 responses to synthetic CB1R agonists**

1102 **a**, Dose-response curves for WIN55212-2 measured in HEK293T cells expressing eCB2.0,  
1103 with the corresponding structure and EC<sub>50</sub> value shown; n = 3 wells each.

1104 **b**, Dose-response curves for CP55940 measured in HEK293T cells expressing eCB2.0,  
1105 with the corresponding structure and EC<sub>50</sub> value shown; n = 3 wells each.

1106

1107 **Extended Data Fig. 4 | Expression and response of eCB2.0 in acute mouse striatal  
1108 slices**

1109 **a**, Two-photon fluorescence images of eCB2.0 expressed in the striatum before (saline)  
1110 and after AEA and AM251 application. Arrows indicate eCB2.0 expressing neurites. Scale  
1111 bar, 10 μm.

1112 **b**, Time course of the change in eCB2.0 fluorescence; where indicated, AEA and AM251  
1113 were applied.

1114

1115 **Extended Data Fig. 5 | eCB and Ca<sup>2+</sup> waves in mouse hippocampal CA1 region during  
1116 seizure activity**

1117 *In vivo* two-photon fluorescence images of eCB2.0 and jRGECO1a expressed in the  
1118 mouse hippocampal CA1 region before and after stimulus evoked seizure activity. Frames  
1119 were extracted from those shown in Supplementary Video 1. Seconds (s) after the stimulus  
1120 are indicated. Scale bar, 100 μm.

1121

1122 **Supplementary video 1 | eCB and calcium signals in mouse hippocampal CA1 during  
1123 seizures**

1124 Fluorescence movies of eCB2.0 and jRGECO1a in the mouse hippocampal CA1 region  
1125 during seizure activity, which is indicated by the LFP recording. The video is played at 3  
1126 times the speed.